Investigating plasma viscosity with fast framing photography in the ZaP-HD Flow Z-Pinch experiment

Jonathan Robert Weed

A thesis
submitted in partial fulfillment of the
requirements for the degree of

Master of Science in Aeronautics & Astronautics

University of Washington

2015

Committee:

Uri Shumlak, Chair

Brian Nelson

Program Authorized to Offer Degree:
William E. Boeing Department of Aeronautics and Astronautics

University of Washington

Abstract

Investigating plasma viscosity with fast framing photography in the ZaP-HD Flow Z-Pinch experiment

Jonathan Robert Weed

Chair of the Supervisory Committee:
Professor Uri Shumlak
William E. Boeing Department of Aeronautics and Astronautics

The ZaP-HD Flow Z-Pinch experiment investigates the stabilizing effect of sheared axial flows while scaling toward a high-energy-density laboratory plasma (HEDLP $>$ 100 GPa). Stabilizing flows may persist until viscous forces dissipate a sheared flow profile. Plasma viscosity is investigated by measuring scale lengths in turbulence intentionally introduced in the plasma flow. A boron nitride turbulence-tripping probe excites small scale length turbulence in the plasma, and fast framing optical cameras are used to study time-evolved turbulent structures and viscous dissipation. A Hadland Imacon 790 fast framing camera is modified for digital image capture, but features insufficient resolution to study turbulent structures. A Shimadzu HPV-X camera captures the evolution of turbulent structures with great spatial and temporal resolution, but is unable to resolve the anticipated Kolmogorov scale in ZaP-HD as predicted by a simplified pinch model.

TABLE OF CONTENTS

LIST OF FIGURES

Figure Number Page

LIST OF TABLES

GLOSSARY

APS: Active pixel sensor, an advancement from older charge-coupled device (CCD) sensor technology.

CAMAC: Computer Automated Measurement And Control

CMOS: Complementary metal-oxide-semiconductor; the “CCD” used in the Canon T2i DSLR.

DSLR: Digital single-lens reflex camera, a classification for the Canon T2i camera.

HEDLP: High energy density laboratory plasma ($>$ 100 GPa)

PLC: Programmable Logic Controller

ICCD: Intensified charge-coupled device used for spectroscopic measurements

MHD: Magnetohydrodynamic

ACKNOWLEDGMENTS

The author would like to sincerely thank Uri Shumlak for his mentorship and for providing the opportunity to research in the ZaP lab, as well as Brian Nelson and Ray Golingo for their valuable discussions and inputs. Thanks are also due to Dzung Tran for his patient instruction in the machine shop, and to Glen Wurden and Todd Rumbaugh for their generous demonstrations of fast framing cameras. Finally, the author is extremely thankful for the immeasurable assistance from Mike Ross, Mike Hughes, and the rest of the ZaP team.

Chapter 1

INTRODUCTION TO PLASMA AND THE ZAP-HD EXPERIMENT

Space exploration is strictly limited by the low thrust and mass efficiency of today's rocket propulsion technology. Chemical devices like solid, liquid, and hybrid rocket engines offer high thrust for launch and rapid orbit transfers, but are plagued by low specific impulses that result in unreasonable mass ratios for distant missions. Electric propulsion devices like ion and Hall effect thrusters have high specific impulse for long duration and station-keeping burns, but their minuscule thrust is unsuitable for getting anywhere quickly to minimize astronaut exposure to harmful radiation. The efficiency limit of a chemical rocket is the quantity of energy stored in the fuel's chemical bonds, while the thrust limit of electric propulsion is the energy harvested from solar arrays, radioisotope thermoelectric generators, or other power plants. Space technology has yet to unleash the extraordinary power of nuclear fusion, which offers an essentially endless supply of potent, clean energy for space propulsion and power plants.

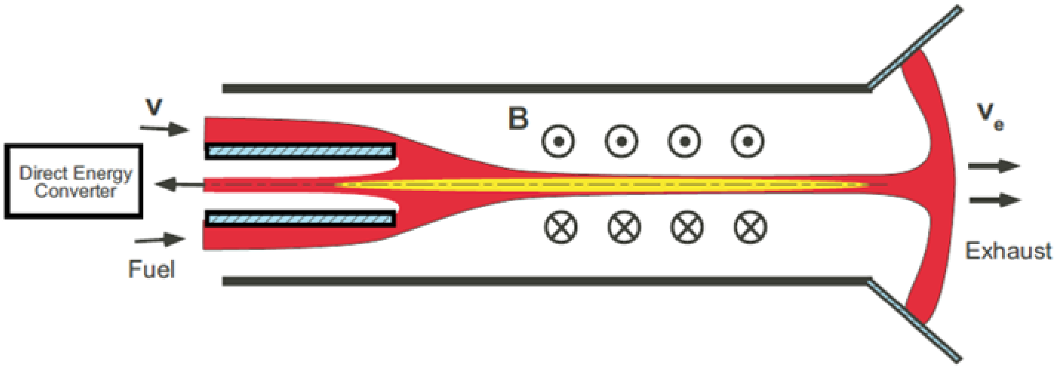

Figure 1.1: Schematic of a nuclear fusion rocket engine based on the ZaP flow Z-pinch concept [10].

Although there are many attractive fusion reactions, the following reaction between deuterium ($^2_1$H) and tritium ($^3_1$H) has the largest nuclear cross section and requires the lowest temperature to initiate:

$$^{2}_{1}\mathrm{H} + {}^{3}_{1}\mathrm{H} \rightarrow {}^{4}_{2}\mathrm{He} + {}^{1}_{0}\mathrm{n} + 17.4\,\mathrm{MeV}. \tag{1.1}$$

However, the Coulomb barrier between the two like-charged hydrogen isotopes is rather strong and requires a great deal of kinetic energy to overcome. In order to achieve net energy production, the Lawson criteria must be met, which is a threshold value for the product of density, time, and temperature ($n\tau T$) and is approximately $3 \times 10^{21} \left[\frac{\mathrm{keV\,s}}{\mathrm{m}^3}\right]$ for the above reaction at a temperature of 14 keV. To reach these conditions, matter must be heated to such extreme temperatures (tens of millions of degrees Celsius) that electrons strip free of atoms to create a quasineutral gas of charged and neutral particles. This state of matter is known as plasma.

1.1 Plasma and the Z-Pinch

The criteria that define an ideal plasma are

1. Quasineutrality: the size of the plasma must be much larger than the distance of diminishing electrostatic influence of charged particles, which is known as the Debye length, or $L \gg \lambda_D$, where $\lambda_D = \sqrt{\frac{\varepsilon_0 k_b T}{ne}}$
2. Collective Behavior: charged particles are coupled through field effects, and the number of particles in a Debye sphere must be large, or $N_D \gg 1$, where $N_D = \frac{4}{3}\pi n \lambda_D^3$
3. Collisionality: the mean free paths of particles must be larger than the Debye length, but smaller than the size of the plasma, or $\lambda_D \ll \lambda_{MFP} \ll L$

Laboratory plasmas are typically produced by a Townsend avalanche, where strong electric fields accelerate free electrons to collide with neutral atoms. These collisions release more free electrons that collide with more neutrals in an ionization cascade. Once ionized, the plasma responds to electric and magnetic fields that can be used to confine it to a vacuum region far away from material walls where the plasma may be heated to fusion temperatures.

The simplest plasma confinement configuration is the Z-pinch, a linear geometry that is found in nature in the form of lightning. In a Z-pinch, electric current compresses or "pinches" the plasma with a self-generated magnetic field (figure 1.2). The electric current and magnetic field together exert a pressure on the plasma through the Lorentz force, $\vec{F} = \vec{j} \times \vec{B}$, where $\vec{j}$ is current density and $\vec{B}$ is magnetic field strength. The plasma pushes back with its own pressure, and an equilibrium is reached where plasma and magnetic pressure are in balance, $\nabla p = \vec{j} \times \vec{B}$, or more specifically, $\frac{d}{dr}\left(p + \frac{B_\theta^2}{2\mu_0}\right) + \frac{B_\theta^2}{\mu_0 r} = 0$.

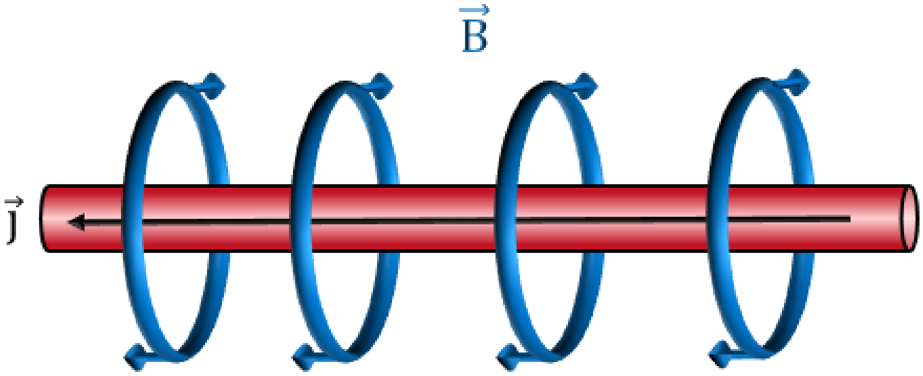

Figure 1.2: The electric current and self-generated magnetic field of a Z-pinch compress plasma through the Lorentz force.

1.2 Plasma instabilities

Like a ball resting on a hill, the Z-pinch is an unstable equilibrium. Specifically, Z-pinches are unstable to the $m = 0$ "sausage" and $m = 1$ "kink" magnetohydrodynamic (MHD) instabilities. The $m = 0$ instability is an axisymmetric constriction that occurs when current concentrates at some point along the length of an inhomogeneous pinch. The magnetic field increases in intensity at this point, further constricting the plasma until the pinch breaks and the circuit opens, terminating plasma confinement. The $m = 1$ instability occurs when current paths distribute the magnetic field asymmetrically about the azimuthal direction, leading to a bowing out of the plasma that further exaggerates until the Z-pinch structure is lost. Since the instability growth times are measured in tens of nanoseconds, their stabilization is necessary for the Z-pinch to approach fusion plasma conditions.

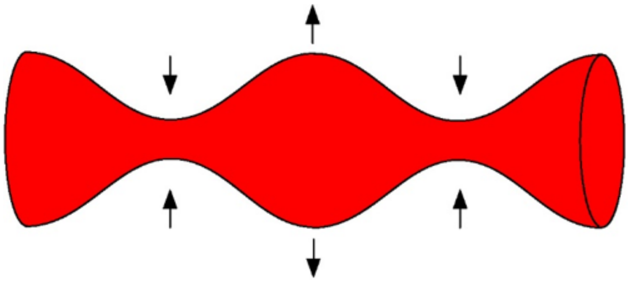

Figure 1.3: The $m = 0$ "sausage" instability.

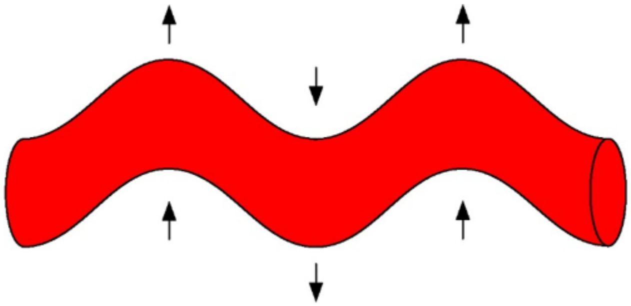

Figure 1.4: The $m = 1$ "kink" instability.

Instability remedies include close conducting walls, gradual pressure gradients, applied axial magnetic fields, and sheared axial flow. Close conducting walls form image currents that counter magnetic field concentrations, but close proximity to materials is not ideal for fusion plasmas. Gradual pressure gradients stabilize the $m = 0$ instability, but do not stabilize the $m = 1$ kink mode [6]. The application of axial fields results in unacceptable end losses and requires additional compression of the axial magnetic field, but is an idea that evolved into the tokamak and other two dimensional magnetic confinement devices that are still widely investigated. The last option, the application of sheared axial flows, is a viable solution to stabilizing the Z-pinch.

A linear analysis suggests that plasma flow with a sufficient velocity gradient $v_Z' \geq 0.1kV_A$ stabilizes the $m = 1$ kink mode, where k is the instability axial wavenumber and $V_A = \frac{B}{\sqrt{\mu_0 \rho}}$ is the Alfvén velocity [12]. Figure 1.5 depicts this theoretical result graphically. Shear flow becomes the primary stabilizing mechanism as a conducting wall is moved further from the pinch.

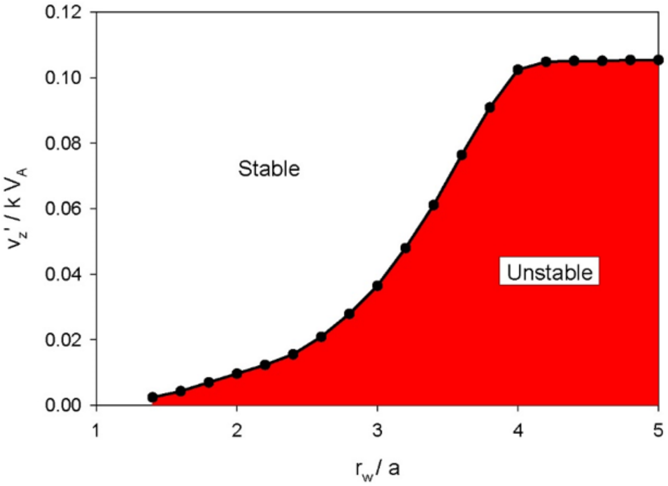

Figure 1.5: Stability criteria for a flow-stabilized Z-pinch: $v_Z' \geq 0.1kV_A$ [12].

Intuitively, sheared flow stabilization may be considered a phase mixing process (figure 1.6). If concentric cylinders of a Z-pinch move with a velocity gradient, instabilities in adjacent layers constructively and destructively interfere. With sufficient shear, the layers are forced to remain axially coherent.

The stabilizing effect of sheared flow has been demonstrated experimentally on the ZaP experiment, as shown in figure 1.7. Velocity gradients correspond to "quiescent" or quiet periods in the plasma when the $m = 1$ mode activity is below a threshold that corresponds to a radial displacement of within one nominal pinch radius. Velocity data are collected with spectroscopy, and mode data are collected with azimuthal arrays of magnetic field probes.

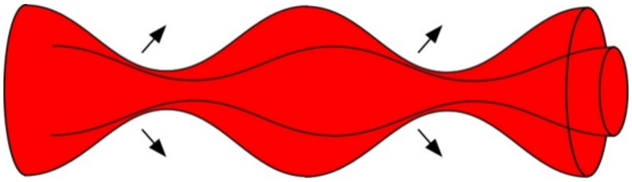

Figure 1.6: Sheared flow stabilization may be considered in the context of phase mixing between concentric cylinders of an unstable equilibrium.

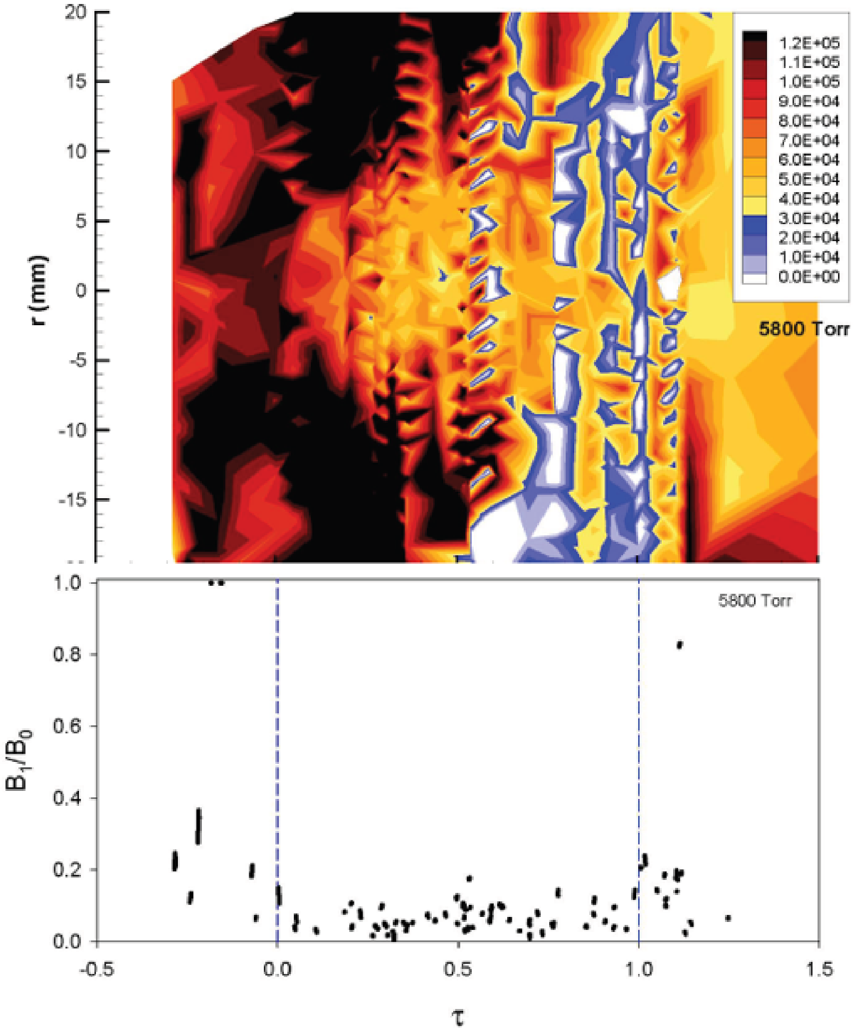

Figure 1.7: The quiescent period is coincident with a sheared flow profile. The top plot depicts radial profiles of flow speeds with respect to the quiescent period ($\tau = [0, 1]$), and the bottom plot indirectly shows radial displacement of the plasma current centroid. The pinch remains quiescent $\left(\frac{B_1}{B_0} \leq 0.2\right)$ while a sufficient velocity gradient exists.

Viscosity is important to the sheared flow stabilization concept because it works to dampen velocity gradients. If sheared flow is attenuated below the stability criteria $v'_Z \geq 0.1kV_A$ in a time faster than the flow-through time of the plasma (the time required for plasma flow to traverse the length of the device), instabilities may resume exponential growth and plasma confinement will be lost. Fortunately, the Z-pinch features favorable density and magnetic field profiles that permit low viscosity in the outer layers of the plasma (see section 3.4), allowing for sufficient endurance of velocity shear to stabilize relatively long flow Z-pinches.

1.3 ZaP-HD experiment

The ZaP-HD experiment investigates the stabilizing effect of sheared flow Z-pinches, and in particular how the concept scales to HEDLP conditions. It is an iteration on the previous ZaP experiment that used coaxial electrodes to form 100 cm, long-lived flow Z-pinches. The ZaP-HD machine employs a triaxial electrode design to separate the plasma formation and acceleration stage (between an inner and middle electrode) from an assembly region where a flow Z-pinch is formed (between an inner and outer electrode). Two separate capacitor banks are used to supply the high voltage (10 kV) and current (150 kA) required to sufficiently ionize a gas (typically hydrogen) to generate a plasma that is accelerated and compressed to form a flow-stabilized Z-pinch with the specifications shown in table 1.1.

The experiment uses a host of diagnostics to measure quantities that reveal the physical parameters of the plasma. Diagnostic access is aided by a slotted outer electrode design that permits a wide viewing angle through rectangular windows on the vacuum vessel and does not affect plasma stability [8]. Diagnostic measurements are performed by:

- Index of refraction measurements: A four-chord HeNe heterodyne-quadrature interferometer measures time resolved electron density, allowing for independent measurements in the acceleration and assembly region, or across the pinch radius. Also, an Nd:YAG holographic interferometer measures spatially resolved electron density that may be processed to generate radial plasma density profiles.

- Spectroscopy: An ICCD spectrometer measures ion temperature and bulk plasma velocity through Doppler shift and Doppler broadening.

- Magnetic field measurement: $\dot{\mathrm{B}}$ probe arrays measure magnetic topology created by plasma currents throughout the experiment, and azimuthal array measurements are Fourier decomposed to their $m = 0$ and $m = 1$ components for plasma stability analysis.

- Voltage and current measurement: High voltage probes, Pearson probes, and Rogowski coils monitor capacitor bank voltages and plasma currents between electrodes.

- Fast framing photography: High speed cameras capture global plasma structure for qualitative understanding and corroboration with other diagnostics, or for the purpose of this thesis, to investigate plasma turbulence.

Quantities	**ZaP**	**ZaP-HD**
Charge Voltage	10 kV	10 kV
Pinch Current	50 kA	150 kA
Pinch Radius	1 cm	2 mm
Density	10^{23} m^{-3}	10^{24} m^{-3}
Ion Temperature	80 eV	720 eV

Table 1.1: The ZaP-HD experiment aims to scale the ZaP flow Z-pinch concept to approach HEDLP conditions.

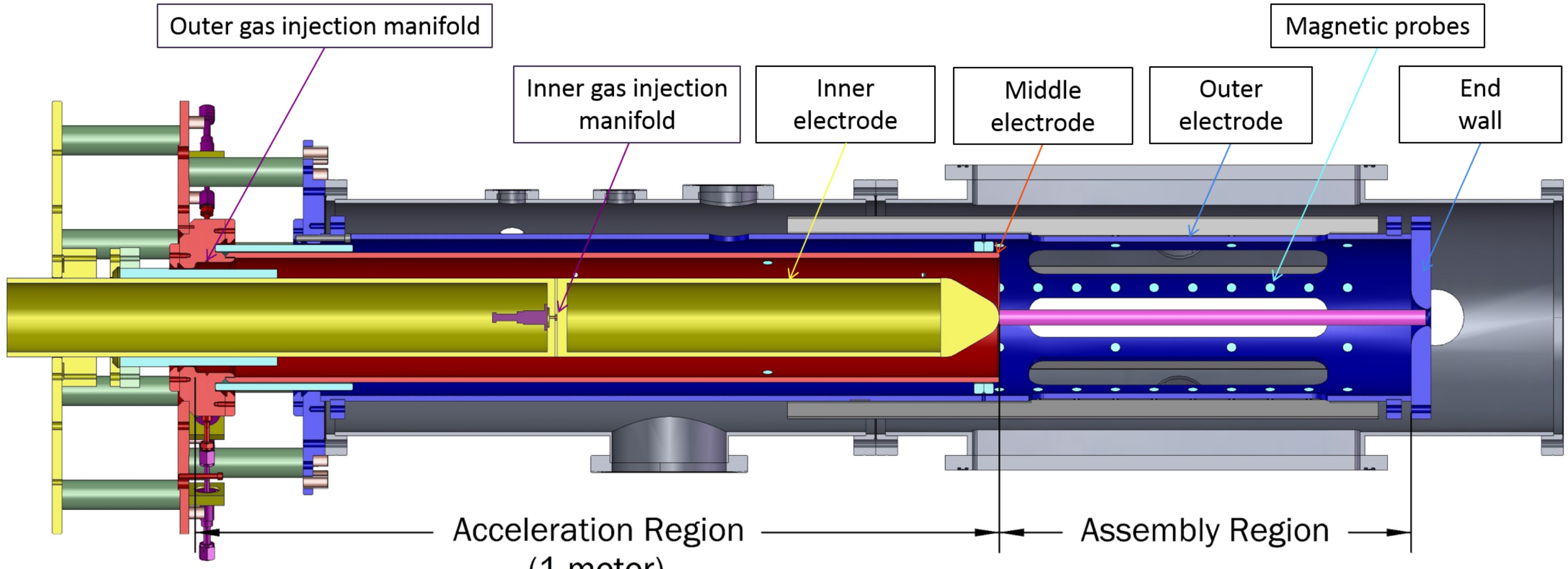

Figure 1.8: The ZaP-HD experiment uses a triaxial electrode design to separate plasma acceleration current between the inner and middle electrodes from pinch current between the inner and outer electrodes in the assembly region. This gives experiment operators separate controls over plasma flow and plasma compression.

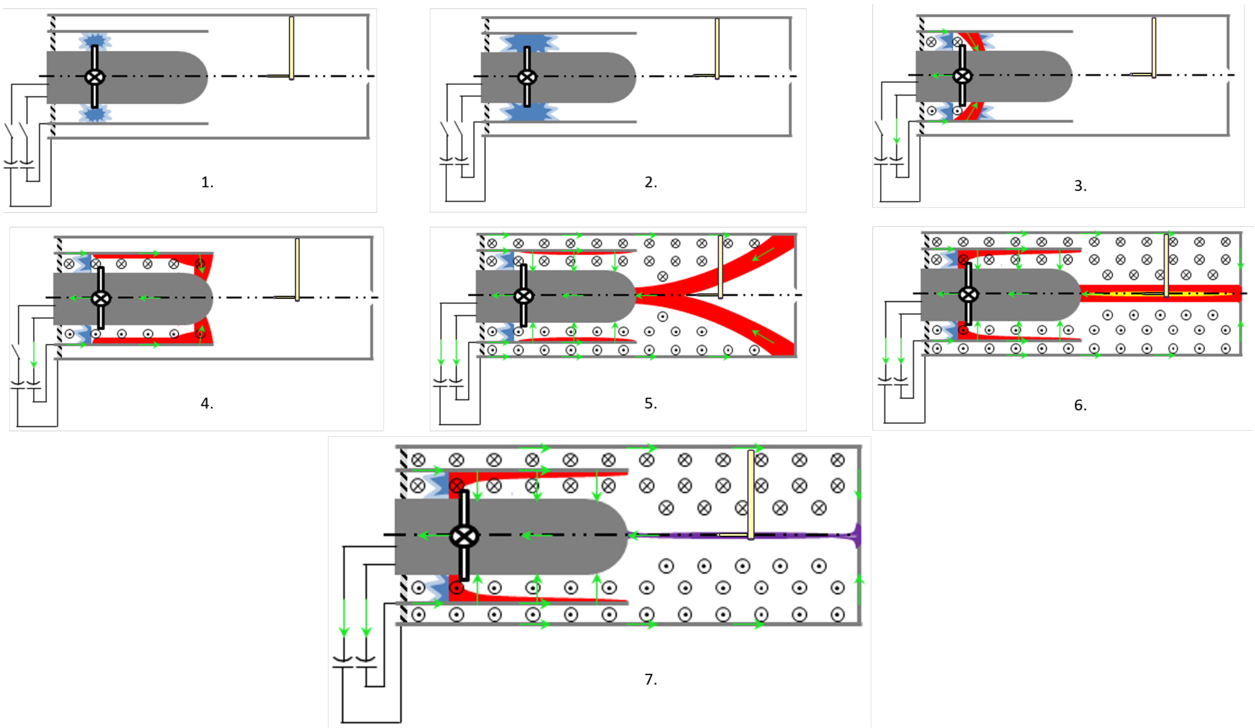

Figure 1.9: Depiction of sheared flow Z-pinch formation with a turbulence tripping probe in position on the dashed Z-axis. Following the initial gas puff (typically hydrogen) and ionization (1-2), the Lorentz force accelerates plasma down the coaxial gun (3-4). A plasma current sheet connects to the outer electrode in the assembly region and is driven to the end wall (5). Current from the outer electrode flows through the plasma, and the associated magnetic field compresses the plasma to form a Z-pinch while high velocity flow (rightward as depicted) from the acceleration region stabilizes the pinch by sustaining a sheared flow profile (6-7). Of interest in this study is turbulence excited in the plasma flow (7).

1.4 Sources of visible light in ZaP-HD

Plasmas are rich with waves, including acoustic, magnetosonic, Langmuir, Alfvén, and electromagnetic waves, the last of which are of interest in this section. Plasmas produce energy at many frequencies across the electromagnetic spectrum, but in ZaP-HD visible light is primarily produced by atomic emission and bremsstrahlung radiation.

Atomic emission or line radiation occurs in a plasma when bound electrons in neutral or ion species drop to a lower quantum mechanical energy level and emit a photon at a precise frequency. In a hydrogen plasma, visible line radiation emits from the Balmer series as shown in figure 1.10. H-α is the most intense atomic emission in the plasma, but other impurities like carbon, oxygen, nitrogen, and boron produce significant line radiation intensities as well.

Figure 1.10: The Balmer series includes H-α and H-β emission, the first and second lines from the right, respectively.

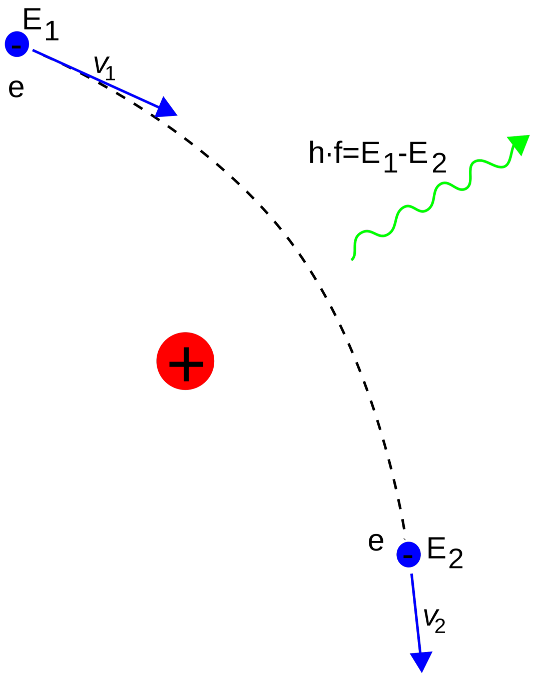

Figure 1.11: Bremsstrahlung radiation occurs when free electrons are decelerated by ions.

As temperature increases, plasmas may reach a threshold where ions are completely stripped of their electrons and no longer emit line radiation. Here, visible light is produced by bremsstrahlung radiation which occurs when free electrons are decelerated after passing in the vicinity of ions. Instead of emission at a specific frequency, bremsstrahlung is continuum radiation that decreases in intensity at higher temperatures but increases in total spectral width. Bremsstrahlung radiation is emitted at all temperatures where free electrons exist, but during this study plasma temperatures are estimated to have remained below 100 eV, and line radiation was the most intense source of visible light produced by the ZaP-HD experiment.

Chapter 2

IMACON FAST FRAMING CAMERA DIGITAL CONVERSION

The ZaP-HD experiment uses a Hadland Imacon 790 fast framing camera to capture time-resolved global plasma structure. The analog camera can capture both framed and streaked images, and the ZaP lab has access to framing units with speeds of 0.5, 1, and 5 million frames per second (FPS). Though the camera was state of the art in its year of manufacture (1986), it has since become obsolete due to its relatively poor resolution and use of Polaroid instant film[1] that is no longer in production and becoming increasingly expensive at approximately $1.00 per photograph in 2014.

A digital conversion was undertaken to eliminate the need for Polaroid film procurement and to provide a method of rapidly separating output frames to better visualize time-resolved plasma dynamics and correlate pixel location with physical locations in the experiment. The resulting modification is shown in figure 2.1. Along with the physical conversion, software was developed to process the output digital images and a system was implemented to run the camera entirely from the experiment's control room. Previously, Polaroid film needed to be extracted from the camera after each experiment pulse, a process that was inconvenient, cumbersome, and prone to user error.

2.1 DSLR camera configuration

To convert the Imacon from analog to digital frame capture, light emitted by the camera's phosphor screen needed to be captured over a long exposure on a digital camera instead of on Polaroid film. The Imacon camera works by directing beams of electrons onto a phosphor screen in a manner similar to a cathode ray tube. The camera uses two transverse electric fields to steer each frame's electron beam onto sequential areas of a phosphor screen. Frames are output in an order shown in

---

[1] This type of film is now only manufactured by Fuji Film, and is slated to end production soon. "Polaroid film" will be used for convenience.

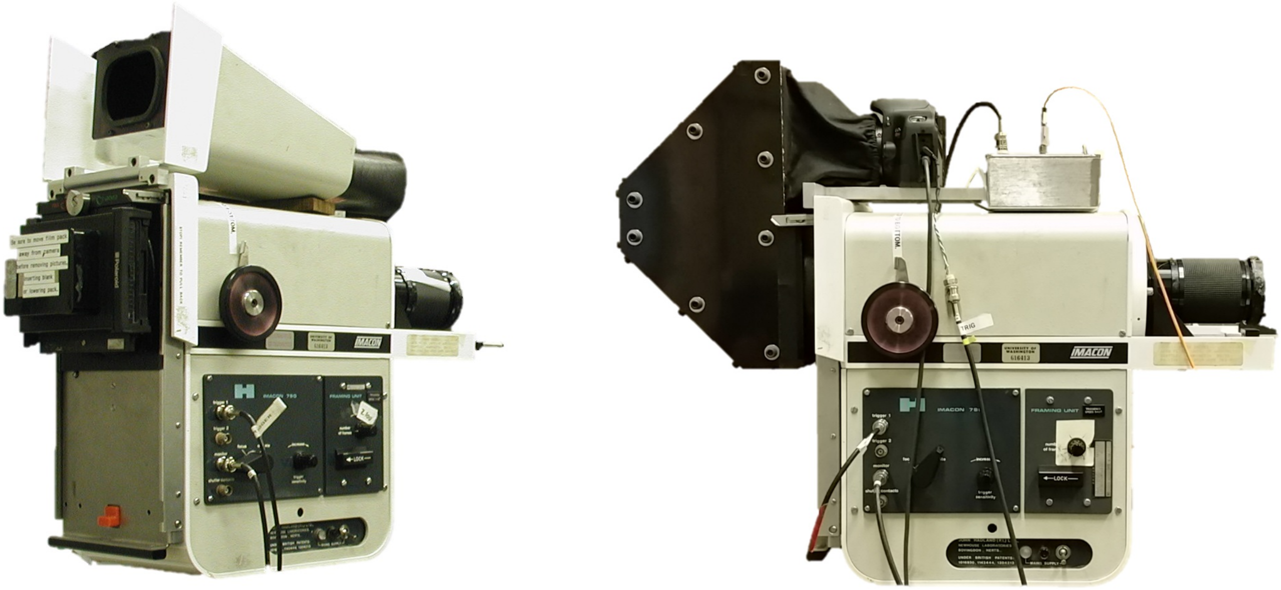

Figure 2.1: On the left is a normal Polaroid film Hadland Imacon 790, while on the right is ZaP-HD's Imacon 790 converted for digital image capture.

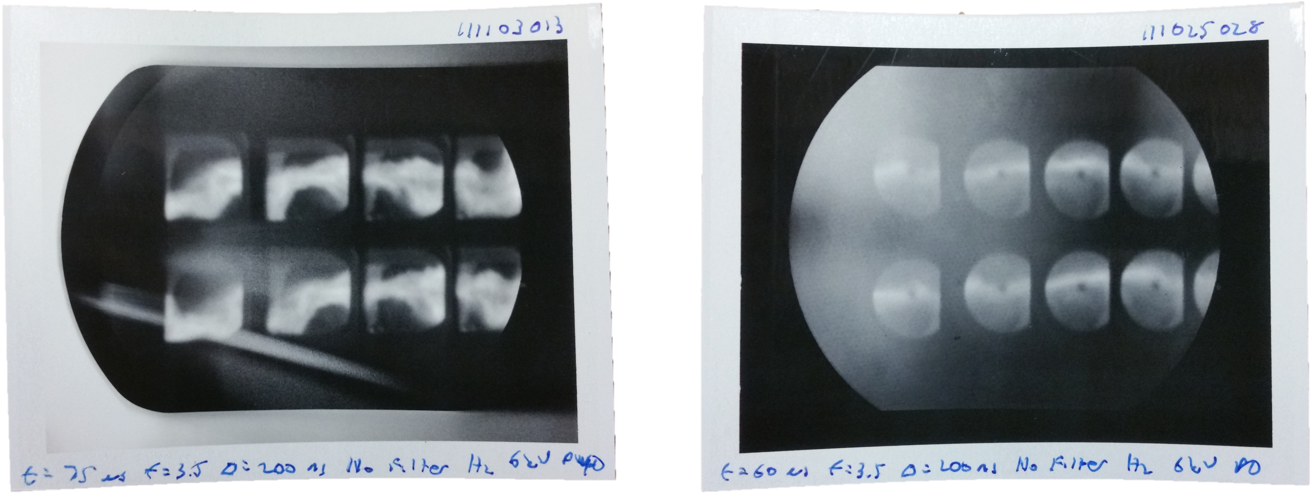

Figure 2.2: Images taken before the digital Imacon conversion. Inconsistent Polaroid film development left some images faded or smeared.

figure 2.3, which requires a high speed oscillator for top/bottom frame deflection and a stepping waveform for horizontal deflection. Though the number of frames displayed on the phosphor screen may be adjusted from 6–16+ frames, 8 frames are typically displayed in order to avoid frame overlap. The phosphor screen uses a type P11 phosphor with output at 460 nm (blue).

Despite the typical brightness of a plasma source and light amplification on the phosphor screen, the short exposures of each frame (20–200 ns depending on the framing unit used) yield low light intensity emitted by the phosphor screen. To evaluate the feasibility of coupling a digital camera to the phosphor screen, trials were held with two cameras. An Olympus C-3030Z point-and-shoot camera was used at first, but the screen's blue light went undetected. Next the experiment's digital holographic interferometry camera, a Canon EOS Rebel T2i DSLR with an 18-55mm f/3.5-5.6 lens, was used. The DSLR successfully detected light from the Imacon phosphor screen over a 3.2 second exposure at an ISO speed of 12800, as seen in figure 2.4. As a result of this test, the digital holography camera was reassigned as the Imacon DSLR.

Though the f/3.5 lens aperture setting captured phosphor screen light, the high ISO speed resulted in noisy images. To enhance light detection and reduce noise, an affordable 50 mm f/1.8 lens was installed, allowing for a lower ISO speed of 3,200. This speed serves as a good compromise between noise reduction pixel dynamic range, whereas lower ISO speeds result in excessively dim images without significantly more noise reduction. The pixel dynamic range at 3,200 also pairs well with the Imacon camera's lens for providing user feedback regarding aperture settings. Dim plasma structures may still be detected in low-power plasma pulses with the Imacon lens set at f/3.5, but during bright plasma shots, the DSLR CMOS blue pixels begin to saturate near the Imacon camera's saturation point and images become washed out and sometimes distorted along the horizontal frame edges to give an illusion of curvature.

The f/1.8 lens requires a minimum focal length of 0.45 m, a parameter that became the driving requirement for the reflection assembly, outlined in section 2.2.

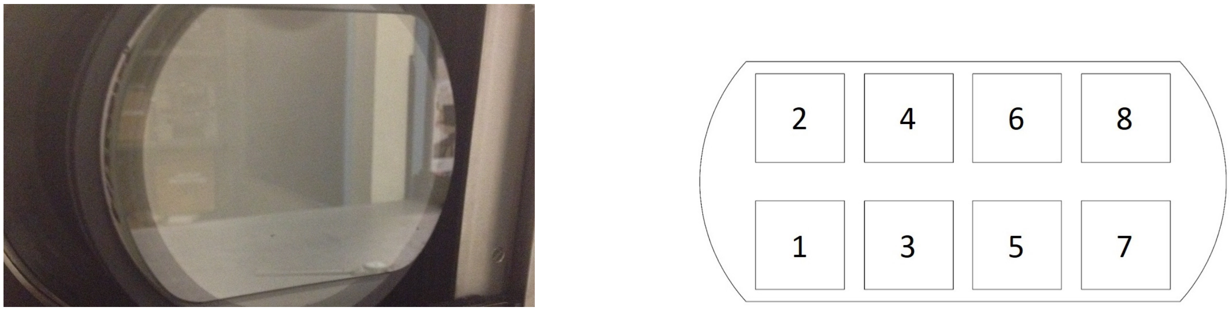

Figure 2.3: Imacon camera phosphor screen and framing sequence. Images are projected sequentially left to right and oscillate from bottom to top.

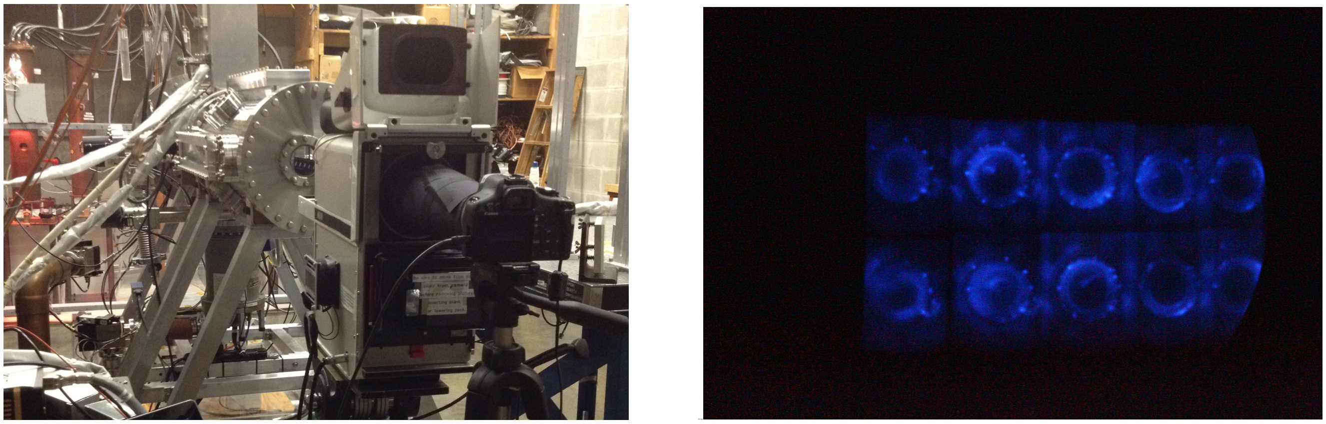

Figure 2.4.a: Imacon with a DSLR camera and a construction paper light enclosure. The view is looking upstream at the middle and inner electrodes from the ZaP-HD vacuum vessel's end flange window.

Figure 2.4.b: Example photo of a 3 kV experiment pulse with the view shown in figure 2.4.a using the f/3.5 zoom lens. This particular exposure packed 10 frames onto the phosphor screen with observable overlap between frames.

Figure 2.4: Initial setup of Imacon camera during trials. These tests determined the viability of capturing phosphor screen light with a digital camera.

2.2 Reflection assembly design and construction

The reflection assembly serves as an interface between the DSLR and the Imacon phosphor screen. It had several design requirements, including:

1. A minimum focal distance of 0.45 m for the 50 mm f/1.8 lens.
2. Compact design with minimal footprint to conserve limited space in the horizontal plane of the lab
3. Provide a light-tight optical path between the phosphor screen and the DSLR lens

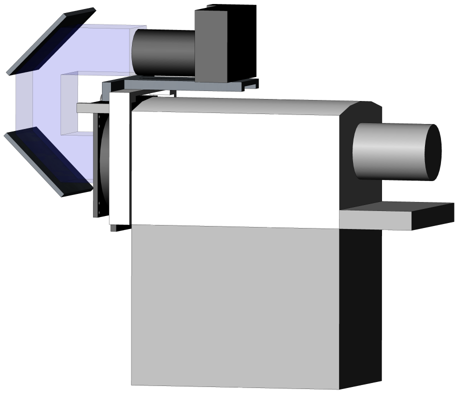

Figure 2.5: Light path for reflecting phosphor screen images to the top of the Imacon camera body, where a DSLR camera is mounted.

To satisfy requirements 1 and 2, light emitted from the phosphor screen needed to be steered away from the phosphor screen to a location with adequate focal distance and where mounting a DSLR camera would be feasible. Since vertical space was not a limiting factor in the lab, the camera was mounted on top of the Imacon camera body using a custom mounting plate. Two mirrors were used to reflect light emitted from the phosphor screen up and around the back side of the Imacon with the light path shown in figure 2.5.

The reflection assembly mirrors were carefully selected to avoid deteriorated image quality. Conventional mirrors consist of a protective glass layer above a reflective surface, a design that works well for perpendicular reflections (as in a bathroom mirror), but with any significant reflection angle tends to produce multiple images due faint reflections from the glass surfaces above the reflecting surface. This effect, known as ghosting, would be detrimental to the image quality at the DSLR. To eliminate ghosting, first surface mirrors were used. These mirrors use a 96% reflective, 0% transparency aluminum coating on the front surface of the glass. Though vulnerable to scratches, the mirrors faithfully reflect the phosphor screen image to the DSLR camera.

The mirrors are held in place at a 45° angle using a custom waterjet-cut aluminum frame that attaches directly to the Imacon polaroid film container mount (figure 2.6). Waterjet cutting was the preferred manufacturing technique as it minimized machining time and allowed for the manufacture of only two large angular frame pieces instead of many small straight aluminum bars connected by fasteners. The angular waterjet-cut shape minimized the weight of the aluminum frame, maintaining the balance of the Imacon camera on its tripod. A heavy reflecting assembly would give the Imacon camera a strong tendency to tilt upward, making the camera cumbersome and difficult to aim. Though ballast weight affixed to the front of the camera could negate balance problems, an elegant Imacon modification was desired, therefore a low-weight reflecting assembly was designed. The front surface mirrors are glued to the aluminum frame with Gorilla Glue ®.

A light-tight environment is maintained by an enclosure consisting of ABS plastic and photographic blackout material (figure 2.7). Custom-cut black ABS plastic panels attach to the aluminum frame with screws, and the inside surfaces of the panels are covered with photographic blackout material to absorb any light that enters the light-tight assembly. The reflection assembly is coupled to the DSLR camera with an interface made from photographic blackout material. The interface is sewn into a cylindrical shape from a single section of cloth, and an elastic hair band was sewn into the fabric on the side of the DSLR to grasp the camera lens. The fabric is glued to the aluminum frame with conventional epoxy and to the plastic panels with plastic epoxy.

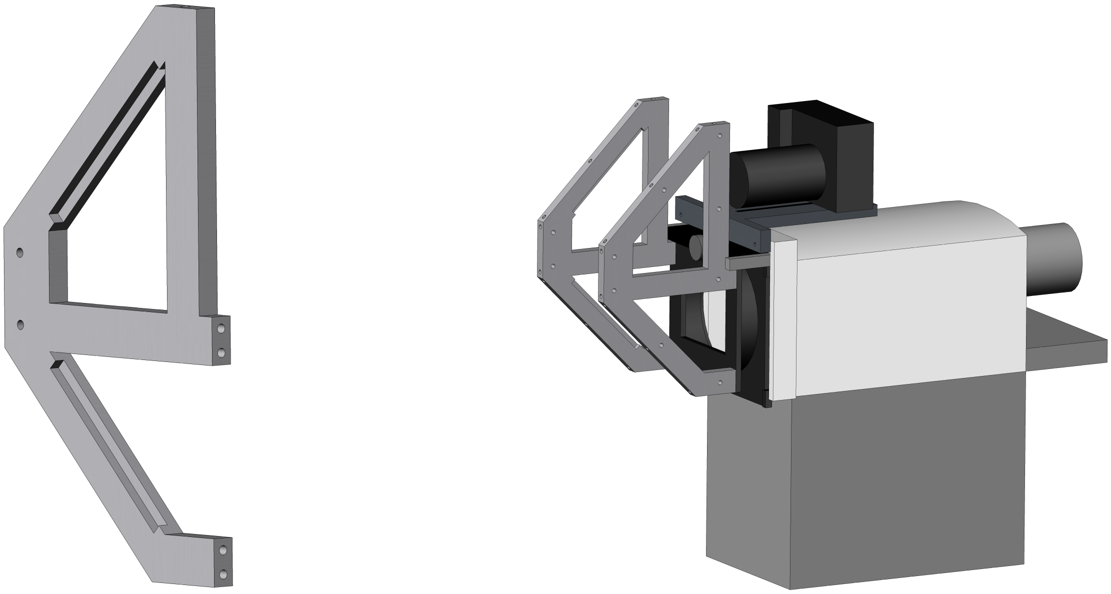

Figure 2.6: Light weight waterjet-cut aluminum frames hold the first surface mirrors and are supported by the Polaroid film container mount. Slots were machined into each frame to cradle the mirrors that are fixed in place with adhesives.

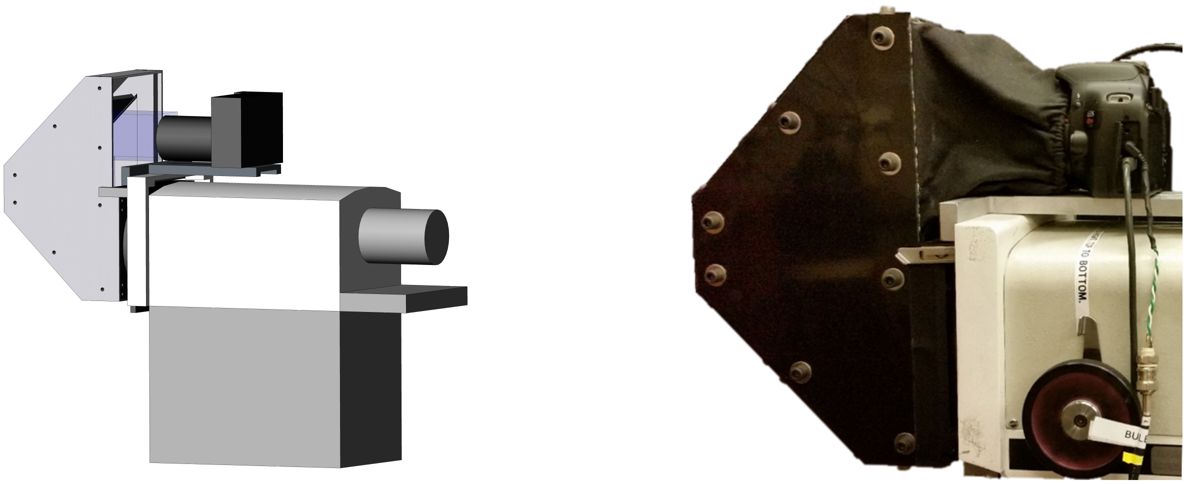

Figure 2.7: Measures to make the reflection assembly light tight include an ABS plastic enclosure and a photographic blackout material interface for the DSLR camera.

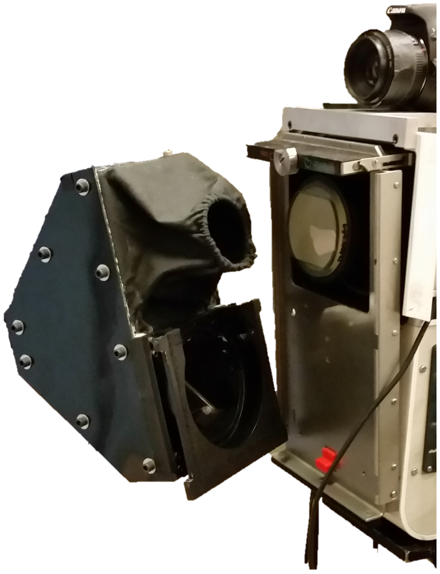

Figure 2.8: Removal of the reflection assembly from the Imacon camera. The circular locking mechanism, hinges, rails, and red button are shown in this image.

The reflection assembly is attached to the Imacon camera using eight #10 screws that extend through the Polaroid film container mount and thread into the reflection assembly aluminum frames. The Polaroid film container mount is set between vertical rails on the back of the Imacon and held in place at the top of the rails with a rotating lock mechanism. Two hinges hold the rails parallel to the back of the Imacon body, but when released tilt the rails to the rear, far enough to allow clear a path for the Polaroid film container mount to slide down on the rails clear of the fragile phosphor screen. If the locking mechanism is rotated counterclockwise after the rails are tilted back, the reflection assembly will slide down the rails. Depressing a red locking button at the bottom of the rails will allow the Polaroid film container mount to slide down the last section of the rail, where it may be removed from the rails. In this manner, the entire reflection assembly may be easily removed from the Imacon camera for maintenance or other reasons, as shown in figure 2.8.

The DSLR is secured to the top of the Imacon camera body by a custom-machined aluminum mount. The mount is attached to the Imacon by two screws that thread into holes formerly used to support a large swing-down viewfinding scope. The DSLR camera is attached to the mount with a

1/4”-20 screw that threads into its tripod mounting hole. The camera is tightly secured into place on the mount as close to the upper mirror as the camera’s minimum focal length allows.

2.3 System operation

As stated earlier, the Imacon camera underwent a digital conversion in part to reduce the workload of experimental operators. The camera is designed to be part of an automated system to capture visible photography of ZaP-HD plasmas. The other parts of the system include a remote trigger for the DSLR shutter, a trigger for the Imacon camera electric shutter, a BNC cable to monitor Imacon framing cycles, an optical USB cable that connects the experiment operational computer to the DSLR camera for photograph download, and MATLAB code that processes photographs by sorting the images and cropping the eight frames of each exposure.

The Canon EOS Rebel T2i is remotely triggered with a wired remote switch (RS-60E3) that connects via BNC cable to a programmable logic controller (PLC), a Koyo Direct LOGIC 205. The remote switch triggers the DSLR shutter by closing a circuit between two of its wires, an operation the PLC accomodates on its F2-04AD-2 module that switches 0–5V DC. The camera shutter is set to be open for 3.2 seconds to cover the experiment pulse and capture the entire glow period of the phosphor screen. The Imacon electronic shutter trigger begins as an electrical signal from a Data Design Corporation DG11A digital delay generator CAMAC module. To reduce electrostatic noise, the signal is converted to an optical signal for its transmission to a trigger box on the Imacon camera where it is converted back to an electrical signal by a photodiode. The trigger box connects to the Imacon camera via BNC cable.

Another BNC cable returns an Imacon monitor signal to a Lecroy TR8837F digitizer and the signal is stored for referencing frame exposure times when corroborating Imacon images with other plasma diagnostics. To reduce magnetically induced noise from a ground loop, the BNC monitor cable serves as the sole ground connection for the Imacon camera (the camera’s power supply is connected to a ground-isolated 120 VAC source).

Once the experiment pulse is complete, images are downloaded to the experiment’s operation computer from the DSLR camera by fiber optic USB (again, to avoid a ground loop). Since the

DSLR camera cannot take photos with a USB cable connected, it is necessary to remotely toggle the power supply of the fiber optic USB cable to enable file transfer after each pulse and disable the connection for image capture in the following experiment pulse. This is accomplished with a KRPA-11DN-24 relay. When provided with a 24 VDC coil voltage via BNC cable from the PLC's F2-08TRS 12–28 VDC module, the relay powers on the fiber optic USB cable and Dropbox ® software uploads the photographs to the experiment's shared cloud drive.

2.4 Imacon code

Once images are uploaded from the DSLR camera to the shared drive, they may be processed with a MATLAB code to improve image presentation. The code's main features are, as shown in figure (2.9):

- 180° image rotation to correct for reflections across two mirrors
- Automated cropping and labeling for the set of 8 frames from the DSLR photographs
- Automated cropping and labeling for each frame from the set of 8 frames
- Production of .gif movies for each experiment pulse

While the products of the code are simple, the implementation of an automated cropping routine was unexpectedly challenging due to the slight variability in the position, size, and brightness of the eight frames on the Imacon phosphor screen between successive exposures. This behavior prohibits the assumption of fixed frame positions in order to avoid frame overlap or missing portions of frames in the cropped output images. Instead, the program uses edge-finding to locate the eight rectangular frames (assumed rectangular with edges parallel to photograph edges, but not assumed collinear in position) and takes advantage of the dramatic jump in blue pixel intensity across the borders of the frames (from approximately zero intensity to the intensity of the object photographed). Since image brightness varies between exposures, the shift in blue pixel intensity

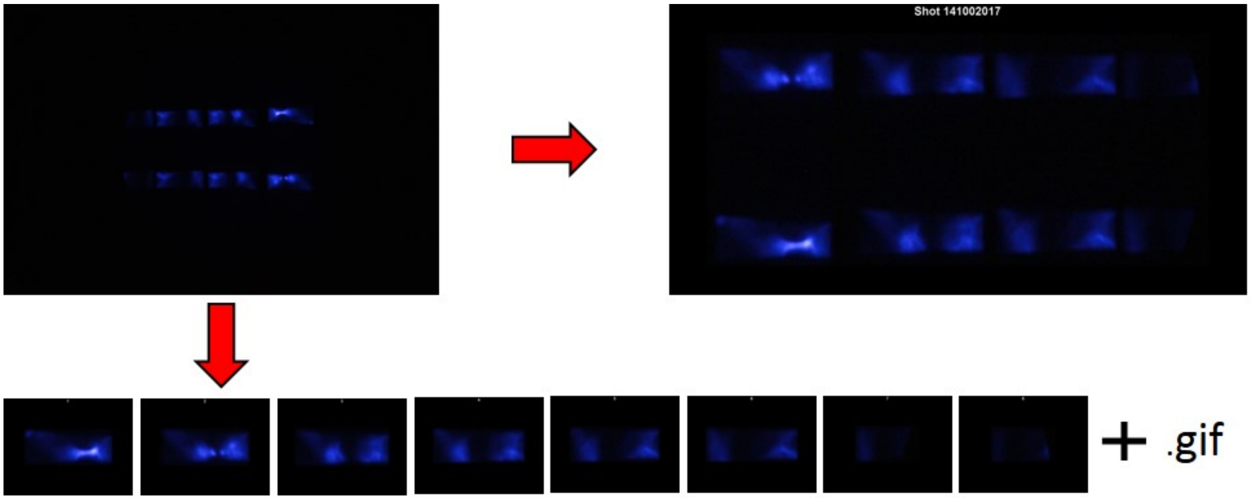

Figure 2.9: Overview of Imacon automated cropping code products: a set of 8 frames, individual frames, and a .gif reel.

across frame edges (i.e., the magnitude of the intensity gradient $\nabla I(x,y)$) also fluctuates. To account for this variability, the program calculates the expected edge intensity using a percentage of each frame's maximum intensity. Furthermore, the code attempts to crop the images using a wide range of expected intensity shifts for both the frames and sets of frames until the cropped output images meet tolerances for overall size, similarity in size (within 20% of average frame dimensions), and other anomalies.

When provided with reasonably bright frames, adequate inter-frame spacing, and continuous plasma structures that appear in each frame, the program successfully outputs cropped images. However, some images may challenge the program's ability to crop the individual frames without user input. Blank or dim images and spasmodic plasma structures were particularly common during the break-in and parameter optimization periods of ZaP-HD, and the program frequently yielded unsatisfactorily-cropped Imacon images. To guard against framing errors the tolerances described above are implemented, but when images do not meet tolerances after several attempts (typically 6) the program abandons automated framing and requests assistance from the user's expert eye.

To manually crop the Images, the program requests that users draw rectangles around the set of 8 frames and around each individual frame. If the selected frame locations are satisfactory to the user, the program runs the rest of the code and saves the frame locations for application to the next image that fails the automated cropping routine. Successive images sometimes have similar frame locations, but frame locations usually shift enough throughout a day of operation to warrant additional user input sessions. If precise frame cropping is not a priority of the operator, the dialog boxes may be clicked through to expedite image processing.

The program includes a feature to detect when the DSLR's blue pixels are excessivley saturated, and only output images from the DSLR's green pixels. This allows operators to still detect structures in the images, even when the Imacon camera's aperture is insufficiently closed. Enabling the feature gives operators a clear indicator (green images) if the camera's f-number needs to be increased. Also available is an option to output cropped frames in a single horizontal sequential image.

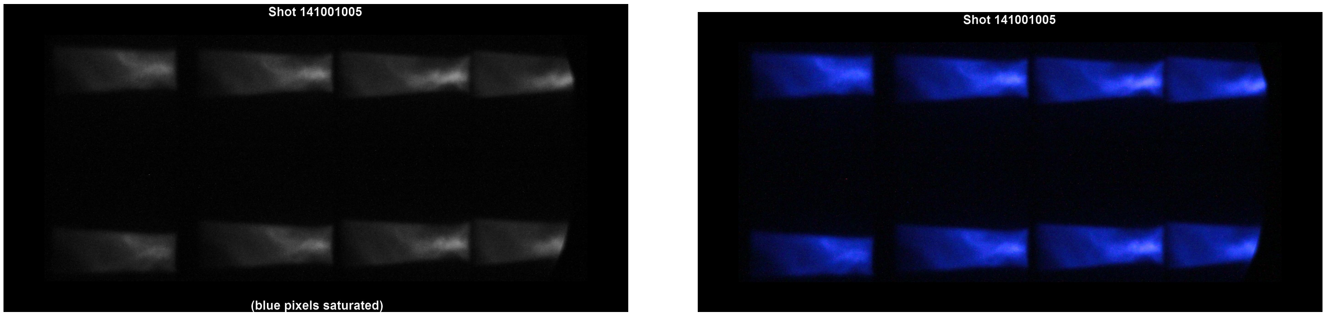

Figure 2.10: Comparison of 8-bit black and white image and color image. The color image has improved aesthetics, dynamic range, and pixel intensity resolution.

Although the program was originally written to output 8-bit black and white images like the Polaroid film photographs, the code was eventually altered to output images in 8-bit color. Color images offered appealing aesthetics, enhanced dynamic range, and improved pixel intensity resolution in images by taking advantage of the DSLR's wide spectral response in red and green pixels (figure 2.10). The DSLR's CMOS sensor consists of a mosaic of red, green, and blue pixels with spectral responses that have considerable overlap, including at the wavelength of the phosphor screen's emission (460 nm). Making the switch to color images dramatically expanded the dynamic range from the 256 intensity values of 8-bit black and white images to a much higher (and difficult to specify) number of intensity values, as indicated in figure 2.11.

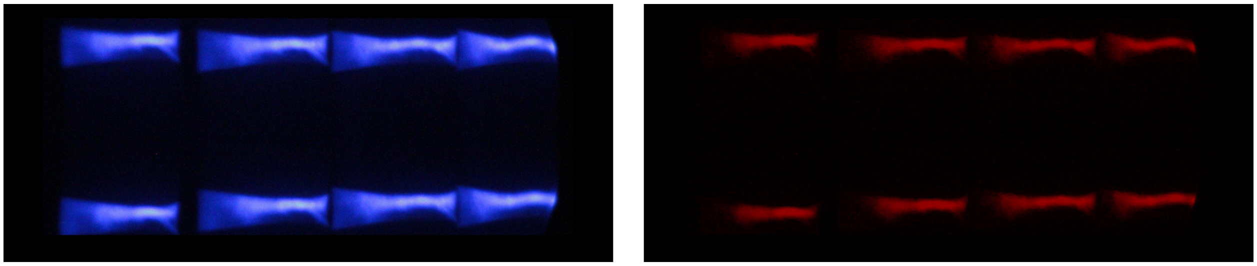

Full Color

Only Red

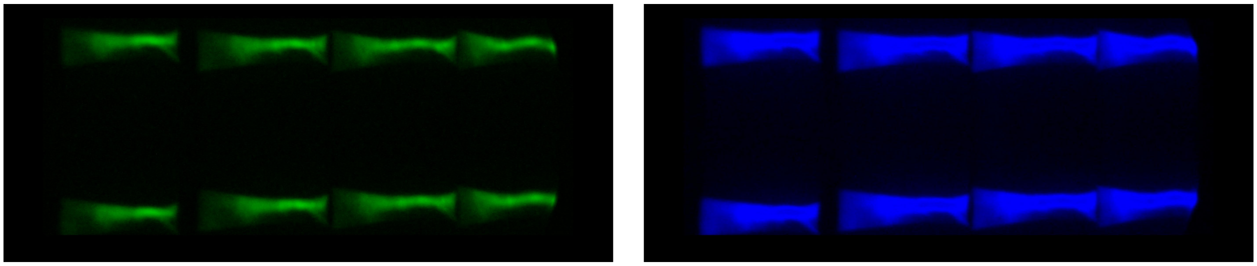

Only Green

Only Blue

Figure 2.11: Imacon images made using only the red, green, and blue pixels of the DSLR. Using all three pixel colors instead of only blue (where the phosphor screen emits) combines the sensitivities of the sensors to 460 nm light. This results in light blue and white colors in the output images where phosphor screen intensity is high.

The output images are compressed (.jpg) files and use approximately 7 MB of storage per shot (when including the set, frames, .gifs, and original image all as separate files). The DSLR can also output images as uncompressed 16-bit images in a proprietary .RAW format, but analysis showed that increased intensity resolution of the .RAW images did not increase the aptitude for edge-finding in the images enough to warrant a file size of 245 MB per shot. Figure 2.12 shows a lineout from an image of the phosphor screen, which is a plot of the intensity of pixels that lie on a line. The lineouts are nearly identical, with similar pixel locations and proportional increases in intensity at the edges of the phosphor screen. This implies that the two formats are interchangeable for plasma structure identification in Imacon images.

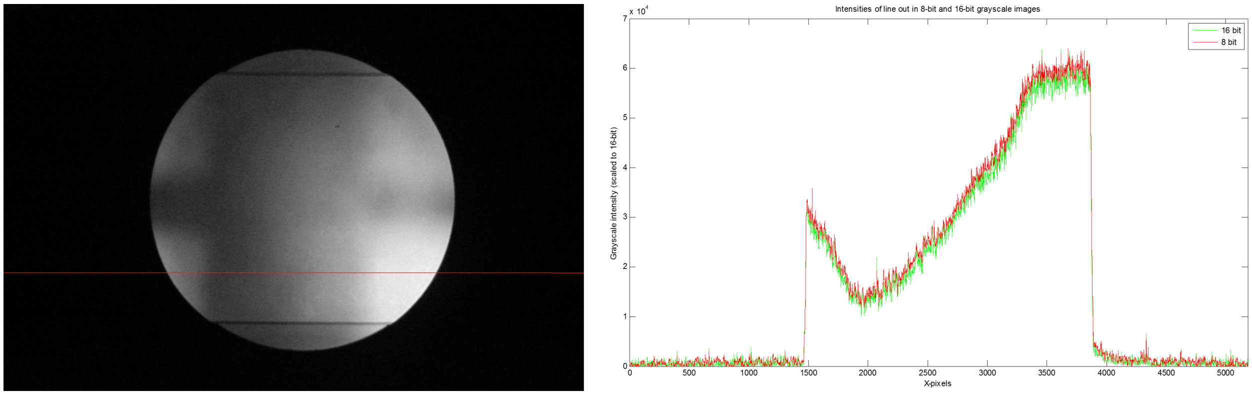

Figure 2.12: A comparison between 8- and 16-bit lineouts reveals similar edge detection performance. The horizontal red line in the photograph is the line chosen for analysis.

2.5 Guest camera comparisons

During the parameter optimization period of ZaP-HD, the lab was fortunate to have two ultra high-speed cameras demoed on the experiment. The cameras revealed plasma structures previously unseen in the ZaP lab and provided the most valuable data for investigating plasma turbulene. The first camera, a Hadland Invisible®Vision Ultra UHSi, was brought from the Los Alamos National Laboratory by Dr. Glenn Wurden; the second camera, a Shimadzu Hypver Vision HPV-X was brought to the ZaP lab by Todd Rumbaugh of Hadland Imaging. Their specifications as witnessed during their demonstrations are summarized in table 2.1.

Figure 2.13 shows an example image from the Ultra UHSi. The camera's image intensifier resulted in grainy images that significantly reduced the advantageous higher resolution of the camera, and the output of only 12 frames made it difficult to follow turbulent structures. Figure 2.14 shows a comparison between the Imacon 790 and the Shimadzu HPV-X. The stark contrast in spatial and temporal resolution made the HPV-X extremely valuable for detecting and tracking the evolution of turbulent structures through 25.6 μs of plasma dynamics at 100 ns intervals. For this reason, it is the source of data used for the remainder of this investigation. Over the course of a two day trial, 12,032 frames (2.3 GB) captured 1.69 ms of plasma dynamics over 48 experimental pulses.

Specification	**Hadland UHSi**	**Shimadzu HPV-X**
Number of Frames	12	256
Resolution	4872x3248	400x250
Max Framing Speed	200M FPS	10M FPS
Min Exposure Duration	5 ns	50 ns
Intensifier Required?	Yes	No

Table 2.1: Comparison of high speed cameras, as demonstrated in the ZaP lab.

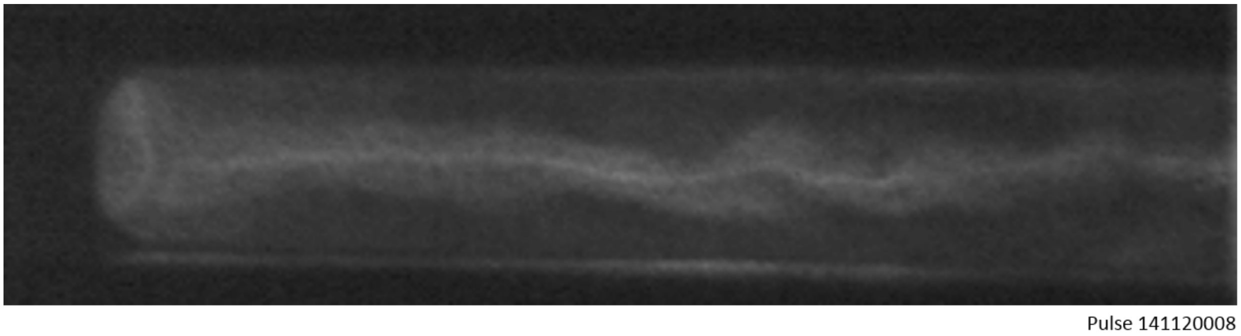

Figure 2.13: The ZaP-HD assembly region, as viewed through the Ultra UHSi.

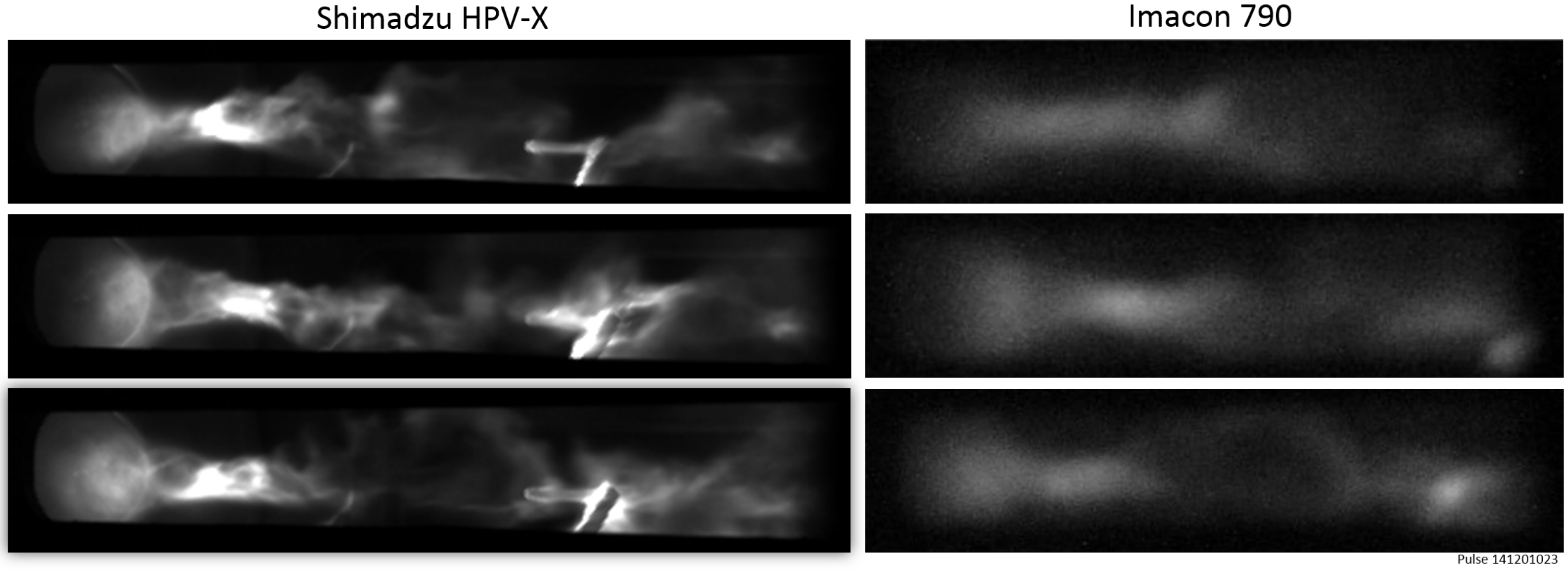
Shimadzu HPV-X

Imacon 790

Figure 2.14: Comparison of simultaneous images from an HPV-X camera (left) and the ZaP lab Imacon 790 (right) with a tripping probe inserted to study plasma turbulence. Both cameras are focused. Higher spatial and temporal resolution unveil plasma structures previously unseen in the ZaP-HD experiment.

Chapter 3

PLASMA TURBULENCE STUDY

3.1 General fluid turbulence

As discussed in section 1.2, plasma viscosity is important for the ZaP-HD experiment, but local viscosity measurements in a plasma are difficult to perform. Conventional instruments like viscometers and rheometers cannot be used in plasma due to its brevity and intense temperature, and determining viscosity indirectly as a function of plasma temperature from spectroscopy and magnetic field strength from $\dot{B}$ probes provides only a global measurement of viscosity. Unfortunately, this is not sufficient for the ZaP-HD experiment where viscosity significantly varies across the pinch radius (along with temperature, density, and magnetic field strength). Instead, this study seeks use visual properties of turbulent plasma flows to make local viscosity measurements.

Turbulence is supremely important to fluid mechanics and an area of ongoing research. Most flows encountered by scientists and engineers are turbulent or have turbulent features due to the low viscosities of everyday fluids like air and water. Developed turbulence is a chaotic process, where flow behavior is extremely sensitive to initial conditions and may only be characterized with repeatable accuracy by stochastic methods. Even then, there are no rigorous statistical theories of turbulence due to a closure problem of the statistical equations, that is, there are always more statistical uncertainties than governing equations. The root of this problem is a nonlinear inertial term in the Navier-Stokes equation that describes fluid flow, both laminar and turbulent. This subtlety in the governing equation for fluid flow results in a rich variety of phenomena at a wide range of time and length scales. Qualitative models of turbulent flow rely heavily on equations not explicitly derived, but rather supported by reason and dimensional analysis. The models give light to universal features and trends that ring true with empirical data and serve as reliable methods to repeatably describe turbulent flows.

Given its nonlinear origins and statistical description, turbulence is a challenging field of research. As a hint of its nature, texts on the subject are garnished with motivational quotes reminding readers of the extreme difficulty (or even suspected futility) of their undertaking. The following study is not intent on completely describing the effects of turbulence in the ZaP-HD, but instead seeks to narrowly use the qualitative behavior of turbulent plasma flow to extract a quantitative parameter, the plasma viscosity. Specifically, the Kolmogorov scales of the turbulent structures and the viscous damping times of the flow are explored in high-speed imagery of the plasma.

3.2 Kolmogorov scale

A brief overview of the Kolmogorov theory of 1941 is necessary background for this study and is the source of the Kolmogorov scale. The central concept of Kolmogorov's theory, the energy cascade, was first proposed by L.F. Richardson. It states that energy in fully developed turbulent flow is passed down from large eddies to small eddies as the larger eddies break apart in a time on the order of their turn-over time ($\frac{l}{u}$), where l is the diameter of the large-scale eddies and u is their average flow velocity. The smaller eddies break apart into even smaller eddies and the process continues until viscous forces become dominant as the Reynolds number approaches unity. At this scale length, known as the Kolmogorov scale η, viscosity converts the kinetic energy of the eddies to thermal energy as they enter the viscous dissipation range. The energy cascade is best summarized by L.F. Richardson himself:

> *Big whirls have little whirls*
> *that feed on their velocity,*
> *and little whirls have lesser whirls*
> *and so on to viscosity.*
> *-L.F. Richardson, 1922*

The "whirls" of Richardson's poem are easy to see but hard to describe. Like the eddies seen in river rapids, an eddy may be defined as a blob of vorticity and its associated rotational and irrotational velocity field, where vorticity is the curl of the velocity field, $\vec{\omega} \equiv \nabla \times \vec{u}$.

A relation for the Kolmogorov scale may be found through dimensional analysis. As given in Pope [9], it is

$$\eta \equiv \left(\frac{\nu^3}{\varepsilon}\right)^{1/4} \tag{3.1}$$

where ν is the kinematic viscosity of the fluid with units $\left[\frac{\mathrm{m}^2}{\mathrm{s}}\right]$ and ε is the rate of dissipation of turbulent energy with units $\left[\frac{\mathrm{m}^2}{\mathrm{s}^3}\right]$. The fluid is assumed to have Newtonian viscosity, where shear stresses are directly proportional to flow velocity gradients through the viscosity coefficient

$$\tau_{ij} = \rho\nu\left(\frac{\partial u_i}{\partial x_j} + \frac{\partial u_j}{\partial x_i}\right) \tag{3.2}$$

$$= 2\rho\nu S_{ij}. \tag{3.3}$$

Here $S_{ij} = \frac{1}{2}\left(\frac{\partial u_i}{\partial x_j} + \frac{\partial u_j}{\partial x_i}\right)$ is the strain rate tensor for two-dimensional flow. ε in equation (3.1) is derived from the Navier-Stokes equation,

$$\frac{D\vec{u}}{Dt} = -\nabla\left(\frac{p}{\rho}\right) + \nu\nabla^2\vec{u} \tag{3.4}$$

where $\frac{D\vec{u}}{Dt} = \frac{d\vec{u}}{dt} + (\vec{u}\cdot\nabla)\,\vec{u}$ is the convective derivative. Multiplying equation (3.4) by $\vec{u}$ gives a fluid kinetic energy equation,

$$\frac{D}{Dt}\left(\frac{\vec{u}^2}{2}\right) = -\nabla\cdot\left[\frac{p}{\rho}\vec{u}\right] + \nu\vec{u}\cdot\left(\nabla^2\vec{u}\right). \tag{3.5}$$

The second term on the right of equation (3.5) deals with viscous dissipation and may be expanded into two terms that are more useful for our purposes. Equation (3.2) is used to show

$$\nu\vec{u}\cdot\left(\nabla^2\vec{u}\right) = u_i\frac{\partial}{\partial x_j}\left[\tau_{ij}/\rho\right]. \tag{3.6}$$

Here the strain rate tensor may be thought of as the rate of strain associated with the smallest eddies is the flow. From the chain rule,

$$\frac{\partial}{\partial x_j}\left[u_i\tau_{ij}\right] = u_i\frac{\partial \tau_{ij}}{\partial x_j} + \tau_{ij}\frac{\partial u_i}{\partial x_j} \tag{3.7}$$

$$= u_i\frac{\partial \tau_{ij}}{\partial x_j} + \frac{1}{2}\left[\tau_{ij} + \tau_{ji}\right]\frac{\partial u_i}{\partial x_j} \tag{3.8}$$

$$= u_i\frac{\partial \tau_{ij}}{\partial x_j} + \frac{1}{2}\left[\tau_{ij}\frac{\partial u_i}{\partial x_j} + \tau_{ij}\frac{\partial u_j}{\partial x_i}\right] \tag{3.9}$$

$$= u_i\frac{\partial \tau_{ij}}{\partial x_j} + \tau_{ij}S_{ij}. \tag{3.10}$$

Substituting equation (3.10) in (3.6) and making use of equation (3.3) for τ_{ij},

$$\nu\vec{u}\cdot\left(\nabla^2\vec{u}\right) = u_i\frac{\partial}{\partial x_j}\left[\tau_{ij}/\rho\right] \tag{3.11}$$

$$= \frac{\partial}{\partial x_j}\left[u_i\tau_{ij}/\rho\right] - \frac{\tau_{ij}S_{ij}}{\rho} \tag{3.12}$$

$$= \frac{\partial}{\partial x_j}\left[u_i\tau_{ij}/\rho\right] - 2\nu S_{ij}S_{ij}. \tag{3.13}$$

Returning to equation (3.5) and applying the convective derivative, we find

$$\frac{\partial(u^2/2)}{\partial t} = -\nabla\cdot\left[\left(\vec{u}^2/2\right)\vec{u}\right] - \nabla\cdot\left[\frac{p}{\rho}\vec{u}\right] + \frac{\partial}{\partial x_j}\left[u_i\tau_{ij}/\rho\right] - 2\nu S_{ij}S_{ij}. \tag{3.14}$$

As shown in Davidson [2],when equation (3.14) is integrated over a volume the first term on the right becomes the rate at which kinetic energy is convected across the volume's boundary, the second is the rate at which pressure forces do work on the volume's boundary, the third is the rate at which the viscous forces do work on the boundary, and the final term represents viscous dissipation of mechanical energy to heat. This is our desired rate of dissipation of turbulent energy, and we conclude $\varepsilon = 2\nu S_{ij}S_{ij}$. ε becomes experimentally accessible by assuming $S_{ij} \approx \frac{\mathrm{v}}{\eta}$, where v is the velocity associated with the smallest eddies in the flow and η is the size of the eddies, a quantity equivalent to the turn-over rate of the eddies. Now,

$$\varepsilon \approx 2\nu\left(\frac{\mathrm{v}^2}{\eta^2}\right). \tag{3.15}$$

In steady turbulence, conservation of energy dictates that the rate of dissipation of turbulent energy must match the rate at which kinetic energy passes down Richardson's energy cascade as the larger eddies break into smaller eddies. This rate, Π, may be quantified by characteristics of the larger eddies, $\Pi \sim \frac{du^2}{dt} \sim -\frac{u^2}{l/u} \sim -\frac{\text{kinetic energy of large eddies}}{\text{turn-over-time of large eddies}}$. Empirical evidence supports that the large eddies break apart on the order of their turn-over-time, and kinetic energy is transferred down the cascade as each eddy breaks up [2]. This yields an energy relationship between the large and small eddies,

$$\Pi \sim \frac{u^3}{l} \sim \varepsilon \approx 2\nu \left(\frac{\mathrm{v}^2}{\eta^2}\right). \tag{3.16}$$

The Reynolds numbers $\left(Re = \frac{ul}{\nu}\right)$ at these two scales differ due to their characteristic lengths and speeds, but at the Kolmogorov scale viscous forces become dominant:

$$Re(\eta) = \frac{\mathrm{v}\eta}{\nu} \equiv 1. \tag{3.17}$$

Combining equations (3.17) and (3.15) yields the Kolmogorov scale (3.18) in a less generalized form than (3.1), carrying over the factor of 2 from the energy dissipation rate ε. In this nebula of approximations, a more useful Kolmogorov scale equation for data analysis is found by substituting the scaling relationship (3.16) for η in equation (3.18).

$$\eta \approx \left(\frac{2\nu^3}{\varepsilon}\right)^{1/4} \tag{3.18}$$

$$\approx 2^{1/4}\left(\frac{\nu^{3/4} l^{1/4}}{u^{3/4}}\right) \approx 2^{1/4}\left(\frac{\mu^{3/4} l^{1/4}}{\rho^{3/4} u^{3/4}}\right) \tag{3.19}$$

$$\sim l\,Re^{-3/4} \tag{3.20}$$

Equation (3.19) is the relation used to evaluate the Kolmogorov scale in this analysis, as it uses scale lengths and velocities that are easily observed in high speed images of the plasma flow. The dynamic viscosity $\mu = \nu\rho$ (with units $\left[\frac{\mathrm{kg}}{\mathrm{m\,s}}\right]$) is substituted for the kinematic viscosity, as plasma density is measured in the experiment with interferometry. These equations also provide a relationship between the smallest and largest eddy velocities,

$$\mathrm{v} = \frac{\nu}{\eta} \tag{3.21}$$

$$\approx \frac{\nu^{1/4} u^{3/4}}{2^{1/4} l^{1/4}} \tag{3.22}$$

$$\approx u\,(2Re)^{-1/4}. \tag{3.23}$$

3.3 Viscous damping time

Another method used in this study to measure plasma viscosity from images is the viscous damping time, that is, the characteristic time for a sheared flow profile to dampen due to viscous dissipation. This parameter was first investigated by the ZaP lab's Sean Knecht for investigating the endurance of a sheared flow profile relative to the flow-through time of the plasma in the experiment [7]. An expression for the viscous damping time is derived from the Navier-Stokes equation by only considering the local variation and diffusion terms,

$$\rho \frac{\partial u}{\partial t} = \mu \nabla^2 u \tag{3.24}$$

which is similar in form to the heat equation. Again, dynamic viscosity is substituted for kinematic viscosity to incorporate density for practical use with experimental data. The equation is normalized about a point such that

$$\tilde{x} = \frac{x}{L} \qquad \tilde{t} = \frac{t}{\tau} \qquad \tilde{\rho} = \frac{\rho}{\rho_0} \qquad \tilde{u} = \frac{u}{u_0}$$

for some characteristic length L, time τ, density ρ_0, and velocity u, assuming uniform viscosity. Substituting these normalized parameters into (3.24), we find

$$\rho_0 \tilde{\rho} \frac{u_0}{\tau} \frac{\partial \tilde{u}}{\partial \tilde{t}} = \frac{\mu u_0}{L^2} \tilde{\nabla}^2 \tilde{u}. \tag{3.25}$$

Since the normalized values are defined to be unity, the non-normalized coefficients may be factored out to develop an expression for viscous damping time.

$$\frac{\tau\mu}{L^2\rho_0}\left[\tilde{\nabla}^2\tilde{u} = \tilde{\rho}\frac{\partial\tilde{u}}{\partial\tilde{t}}\right] = 1 \tag{3.26}$$

$$\tau = \frac{L^2\rho_0}{\mu} \tag{3.27}$$

As an aid for intuition, it is helpful to put equation (3.27) in the context of Couette flow where a linear sheared flow profile exists between two plates, one stationary and one with velocity u (figure 3.1). In this case, L is the distance between the two defining ends of the sheared flow profile and τ would be the time required for the magnitude of the gradient to be reduced by a characteristic portion (such as an e-folding) of its exponential decay.

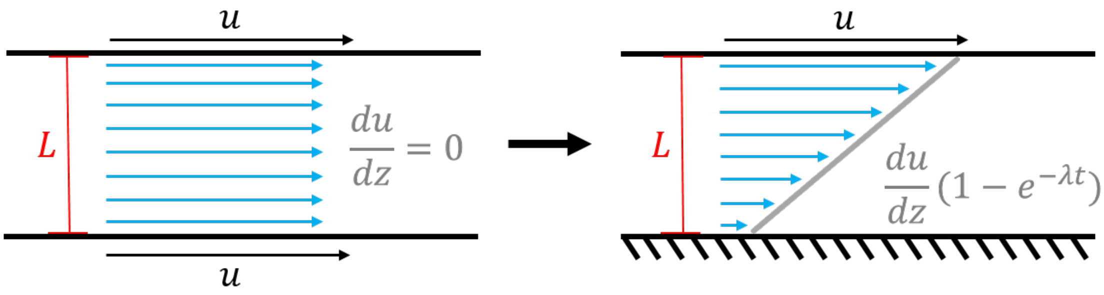

Figure 3.1: In Couette flow, two parallel plates with spacing L, one stationary and one with velocity u, create a sheared flow with velocity gradient $\frac{du}{dz}$. The gradient is asymptotically approached from a uniform flow condition in one characteristic viscous damping time.

An important nuance of the viscous damping time is that it is a purely laminar phenomenon. The expression is obtained by disregarding the convection and specific thermodynamic work terms in the Navier-Stokes equation which enable turbulent flows. Therefore, it is not accurate for use in flows where turbulence is the dominant sheared flow damping mechanism.

3.4 Braginskii viscosity

The viscosity of plasma in the presence of a net magnetic field requires a different relation due to resistance of the fluid's motion across magnetic field lines, where the Lorentz force acts on particles in a direction perpendicular to both their velocity and the magnetic field line. The resultant trajectories are gyrations about the magnetic field lines. However, the Lorentz force only affects motion in the plane perpendicular to the magnetic field lines; motion is unhindered along the magnetic field lines. The Lorentz force gives the diffusion of momentum, and therefore viscosity, anisotropy. A full description of plasma viscosity requires five anisotropic viscosity coefficients, but proper assumptions boil these down back to one coefficient that is chiefly dependent on ion density, ion temperature, and magnetic field strength due to a magnetic field's interference with momentum diffusion.

Unmagnetized dynamic viscosity is derived by Braginskii [1]. It is

$$\mu = 0.96 n_i T_i \tau_{ii} \tag{3.28}$$

$$= \frac{0.406 m_i^{1/2} \left(k_b T_i\right)^{5/2}}{Z^4 e^4 \ln\Lambda} \tag{3.29}$$

with units CGS-K $\left[\frac{\mathrm{g}}{\mathrm{cm\,s}}\right]$. n_i is the ion density, T_i is ion temperature [K], τ_{ii} is the ion collision time[1], m_i is the ion mass, k_b is Boltzmann's constant[2], Z is the charge state, e is the elementary charge[3], and $\ln\Lambda$ is the Coulomb logarithm, a ratio of the effectiveness of small-angle to large-angle collisions[4].

Generally, equation (3.29) shows that the viscosity of unmagnetized plasma is directly dependent on temperature, which is an effect of a longer mean free path $\left(\lambda_{\mathrm{mfp}}\right)$. Although ion density in

---

[1] $\tau_{ii} = \frac{1}{\nu_{ii}} = \frac{4.8\times10^{8}\left(\frac{m_i}{m_p}\right)^{1/2} T_i^{3/2}}{Z^4 n_i ln\Lambda}$

[2] $k_b = 1.381\times10^{-16}\ \left[\frac{erg}{K}\right]$

[3] $e = 4.803\times10^{-10}\ [Fr]$

[4] $\ln\Lambda = \ln\left(6\pi n_{i_{mks}}\lambda_D^3\right) = \ln\left(6\pi n_{i_{mks}}\left(20\times10^{-6}\sqrt{\frac{T_{i_{eV}}}{n_{i_{mks}}/1\times10^{17}}}\right)^3\right)$ where λ_D is the Debye length

equation (3.28) is negated by the ion density dependence in the denominator of τ_{ii}, the temperature dependence makes $\mu \sim T_i^{5/2}$. Strangely, higher temperatures result in lower collision frequencies due to smaller collision cross sections. The ion-ion collision cross-section σ_{ii} may be estimated from $\sigma_{ii} \approx \frac{\nu_{ii}}{n_i u_i}$ as shown in Goldston [5], where ion velocity $u_i \sim T_i^{1/2}$. Since $\nu_{ii} \sim \frac{n_i}{T_i^{3/2}}$ it follows that $\sigma_{ii} \sim T_i^{-2}$. Increasing ion temperature significantly reduces ion collision cross section and increases $\lambda_{\text{mfp}} = \frac{1}{n_i \sigma_{ii}}$. This means ions have more "reach" between collisions, which has the effect of greater momentum diffusion throughout the fluid, translating to higher viscosity.

In the presence of a magnetic field (strong enough such that the ion gyro frequency is much greater than the ion collision frequency), the viscosity perpendicular to the magnetic field is given by Spitzer [13],

$$\mu_\perp = \frac{2}{5}\left(\frac{\pi}{m_i k_b T_i}\right)^{1/2} \frac{Z^4 e^4 n_i^2 \ln\Lambda}{\omega_{ci}^2} \tag{3.30}$$

$$= 2.68 \times 10^{-26} \frac{A_i^{3/2} Z^2 n_i^2 \ln\Lambda}{T_i^{1/2} B^2} \qquad \left(\text{for } \frac{\omega_{ci}}{\nu_{ii}} \gg 1\right) \tag{3.31}$$

again in CGS-K. ω_{ci} is the ion cyclotron frequency[5] and A_i is the ion atomic number (=1 for hydrogen). Interestingly, perpendicular viscosity has an inverse dependence on temperature and an additional quadratic inverse dependence on magnetic field strength. As B increases, ion motion is increasingly dominated by gyrations about magnetic field lines due to the Lorentz force, and there is less ability for the ions to diffuse momentum [4]. Since $\frac{\omega_{ci}}{\nu_{ii}} \gg 1$, the ion spends most of its time within a Larmor radius, as though it were tangled.

Similar to unmagnetized viscosity, the mean free path increases as temperature increases, but in the magnetized case the ion trajectory is restricted to the ion gyro orbit circumference (i.e. not truly "free"). A lower collision frequency at higher temperatures $\left(\nu_{ii} \sim T_i^{-3/2}\right)$ paired with an only somewhat larger gyroradius $\left(r_g \sim T^{1/2} \ll u_i \tau_{ii}\right)$ inhibit momentum diffusion in the plasma, thereby lowering perpendicular viscosity.

---

[5] $\omega_{ci} = \frac{ZeB}{m_{i_{cgs}} c}$

Braginskii [1] offers a less conceptually accessible expression for viscosity that bridges the gap between Braginskii unmagnetized and Spitzer magnetized viscosity. For the ZaP-HD experiment, the most important and variable viscosity is with respect to the radial sheared flow profile $\frac{\partial u_z}{\partial r}$. In Cartesian coordinates, this gradient may be considered as part of a 2-D slice of the cylindrical pinch, where B_θ is aligned with $\hat{z}$, downstream flow is in the $\hat{x}$ direction, and $\hat{y}$ is aligned with $\hat{r}$ as shown in figure 3.2. In these coordinates the velocity gradient of interest is $\frac{\partial u_x}{\partial y}$. The Braginskii stress tensor (similar to equation (3.2)) is $\pi_{\alpha\beta} = -\eta_0 W_{0_{xy}} - \eta_1 W_{1_{xy}} - \eta_2 W_{2_{xy}} + \eta_3 W_{3_{xy}} + \eta_4 W_{4_{xy}}$ where η_p are the five anisotropic Braginskii viscosity coefficients. $W_{p_{xy}}$ are tensors that may be expanded as

$$
\begin{aligned}
\pi_{\alpha\beta} = &- \eta_0 \begin{bmatrix} \frac{1}{2}\left(W_{xx}+W_{yy}\right) & \mathbf{0} & 0 \\ \mathbf{0} & \frac{1}{2}\left(W_{xx}+W_{yy}\right) & 0 \\ 0 & 0 & W_{zz} \end{bmatrix} - \eta_1 \begin{bmatrix} \frac{1}{2}\left(W_{xx}-W_{yy}\right) & \mathbf{W_{xy}} & 0 \\ \mathbf{W_{yx}} & \frac{1}{2}\left(W_{xx}-W_{yy}\right) & 0 \\ 0 & 0 & 0 \end{bmatrix} \\
&- \eta_2 \begin{bmatrix} 0 & \mathbf{0} & W_{xz} \\ \mathbf{0} & 0 & W_{yz} \\ W_{zx} & W_{zy} & 0 \end{bmatrix} + \eta_3 \begin{bmatrix} -W_{xy} & \mathbf{\frac{1}{2}\left(W_{xx}-W_{yy}\right)} & 0 \\ \mathbf{\frac{1}{2}\left(W_{xx}-W_{yy}\right)} & W_{xy} & 0 \\ 0 & 0 & 0 \end{bmatrix} \\
&+ \eta_4 \begin{bmatrix} 0 & \mathbf{0} & -W_{yz} \\ \mathbf{0} & 0 & W_{xz} \\ -W_{zy} & W_{zx} & 0 \end{bmatrix}
\end{aligned}
\tag{3.32}
$$

but only terms in bold are considered when $(\alpha\beta) = (xy)$ for the x-y stress, simplifying the expression to $\pi_{xy} = \pi_{yx} = -\eta_1 W_{xy} + \frac{\eta_3}{2}\left(W_{xx} - W_{yy}\right)$. Here, W_{xy}, W_{xx}, and W_{yy} are rate of strain tensors,

$$W_{xy} = \frac{\partial U_x}{\partial y} + \frac{\partial U_y}{\partial x} - \frac{2}{3}\delta_{xy}\nabla\cdot\vec{u} \tag{3.33}$$

$$W_{xx} = 2\frac{\partial U_x}{\partial x} - \frac{2}{3}\delta_{xx}\nabla\cdot\vec{u} \tag{3.34}$$

$$W_{yy} = 2\frac{\partial U_y}{\partial y} - \frac{2}{3}\delta_{yy}\nabla\cdot\vec{u}. \tag{3.35}$$

Assuming the plasma experiences no compression stresses in the x and y directions, equations (3.34) and (3.35) equal zero, and $\nabla \cdot \vec{u} = 0$. Furthermore, $\frac{\partial U_y}{\partial x}$ is assumed to be zero since radial flow velocity is assumed to be negligible along the length of the pinch. This leaves us with a simplified Braginskii stress tensor, $\pi_{xy} = -\eta_1 W_{xy}$, which for the purposes of ZaP-HD becomes $\pi_{xy} = -\eta_1 \frac{\partial U_x}{\partial y}$ where

$$\eta_1 = \frac{n_i T_i \tau_{ii} \left(\frac{6}{5} \left(2\omega_{ci}\tau_{ii}\right)^2 + 2.33 \right)}{\left(2\omega_{ci}\tau_{ii}\right)^4 + 4.03 \left(2\omega_{ci}\tau_{ii}\right)^2 + 2.33}. \tag{3.36}$$

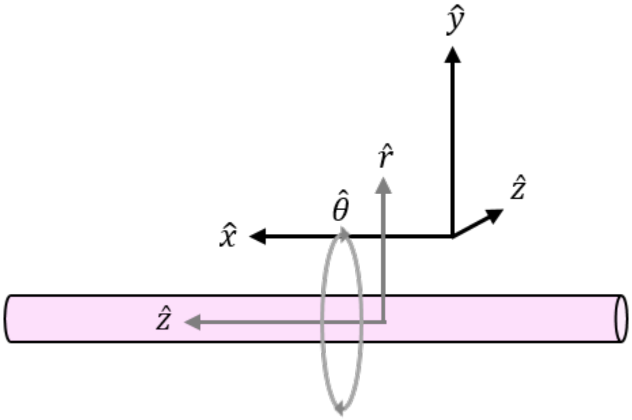

Figure 3.2: Coordinate system used for Braginskii viscosity coefficient determination.

As shown in figure 3.3, equation (3.36)'s polynomial form gracefully links Braginskii unmagnetized and Spitzer magnetized viscosity. Each term with $\omega_{ci}\tau_{ii}$ serves as a "degree of magnetization". As B approaches zero, so does $\omega_{ci}\tau_{ii}$, approximately resulting in Braginskii unmagnetized viscosity (3.28).

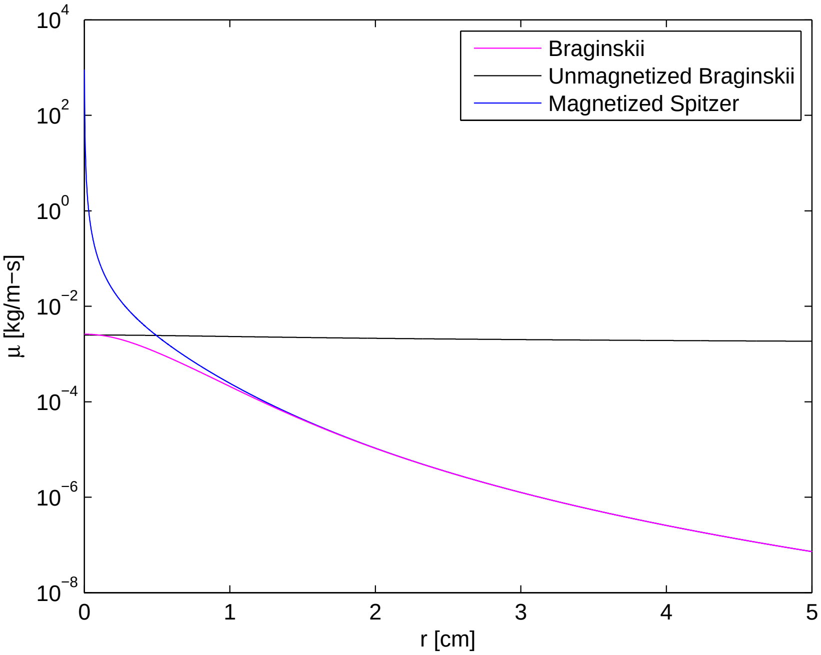

Figure 3.3: Comparison of viscosities across a Z-pinch radial profile.

3.5 Turbulence tripping probe

To excite small length scale turbulence in the ZaP-HD flow Z-pinch, turbulence tripping probe was developed. The probe was designed to introduce turbulence through by creating boundary layer flows around a small diameter sting and creating secondary wake flows around a larger mast. The tripping probe is made of Saint-Gobain grade AX05 high purity boron nitride, a ceramic material with a melting point greater than 2000 °C that allows the probe to withstand brief exposures to hot plasmas on the order of 1 million °C. With a consistency similar to chalk, boron nitride is easily machinable but extremely fragile. Though it quickly absorbs atmospheric moisture, the material performs favorably under vacuum after a period of off gassing in a vacuum oven. Boron nitride has a high dielectric strength (79 kV/mm) that denies a current path between the plasma and the experiment's vacuum tank to which the tripping probe is mounted.

The tripping probe sting, a 3 mm (1/8") diameter boron nitride rod with a rounded tip, extends

3.2 cm (1.25”) upstream from the mast location at P23, which is approximately one half the length of the assembly region. It is attached to the 6 mm (1/4”) diameter, 15.2 cm (6”) long mast by a vented stainless steel set screw that threads into the most downstream 1.3 cm (1/2”) of the sting and the tip of the mast. On the tip of the mast, a flat circular surface is milled around the set screw’s threaded hole to allow the butt of the tripping probe sting to rest flush against the mast so that the sting may extend upstream parallel to the Z-axis.

The boron nitride mast connects to a copper adapter that serves as an interface between the boron nitride mast and a linear translator. The adapter gently clamps the boron nitride mast in place while avoiding trapped gas volumes, and a stainless steel screw through a clearance hole in the boron nitride mast serves as a redundant measure to secure the mast in place. When the linear translator is extended approximately 13.8 cm (5.43”) such that the tripping probe sting lies on the Z-axis, the adapter remains 2.5 cm (1.0”) beyond the exterior surface of the outer electrode, clear of plasma currents that could conduct through the copper adapter and stainless steel linear translator to the vacuum tank. When the linear translator fully is retracted, the tripping probe sting stays clear of the outer electrode outer diameter by 2.5 mm (0.1”) to avoid disrupting plasma flows.

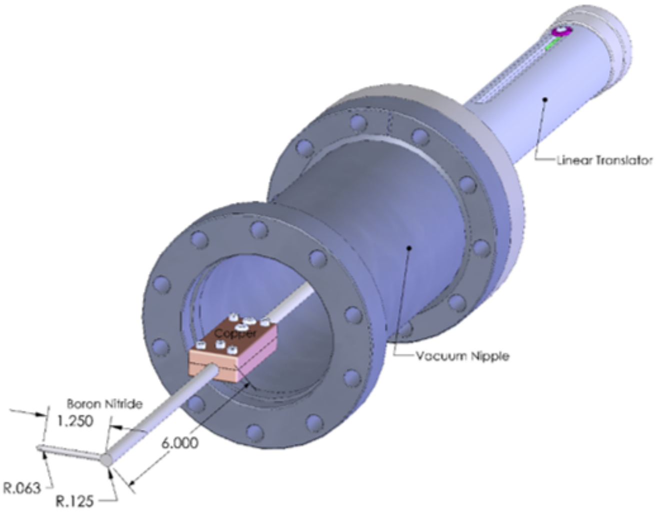

Figure 3.4: Schematic of the ZaP-HD turbulence tripping probe. A small diameter sting extends 3.2 cm (1.25”) upstream of a 15.2 cm (6”) mast, which is connected to linear translating assembly.

The fragility of the tripping probe assembly cannot be overemphasized, as shown in figure 3.5. The accident occurred while attempting to screw the sting into the mast using a stainless steel set screw. As a word of caution, the application of seemingly negligible torque runs a high risk of fracturing the thin boron nitride cylinder that surrounds the stainless steel set screw.

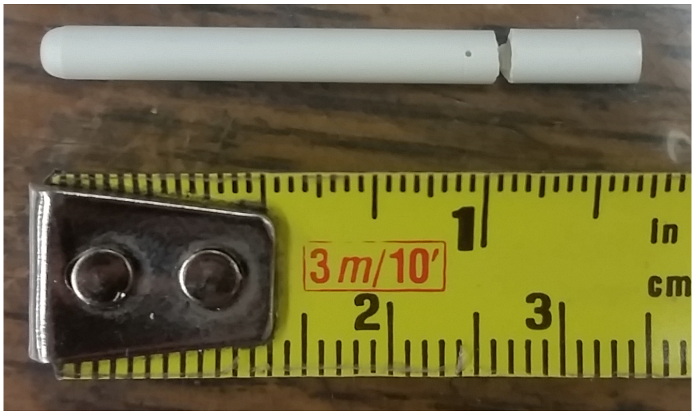

Figure 3.5: A fractured boron nitride tripping probe sting.

Chapter 4

THEORETICAL PREDICTIONS AND EXPERIMENTAL RESULTS

The Kolmogorov scale is explored by tracking and measuring the smallest light-emitting structures produced by turbulent interactions with a turbulence tripping probe. To measure viscous damping time, only laminar interactions with the turbulence tripping probe are considered, of which there were few. The data were collected during a period of experimental optimization when the parameter space for variables like inner and outer gas puff times, acceleration and compression capacitor bank delay times, and capacitor bank voltages had not yet been fully characterized. As a result, well-confined Z-pinches were highly spasmodic. Fluctuating density and azimuthally asymmetric structures resulted in “strikes” with the turbulence tripping probe, where discrete light-emitting structures or “blobs” impacted the probe and produced turbulent structures with dwindling size that evolved into diffuse flow. Viscous dissipation may be responsible for their reduction in size, or perhaps the structures rapidly cool once severed from an electric current path.

To discern whether the identified structures were associated with the Kolmogorov scale, the pinch is modeled with reference to experimental measurements to characterize the plasma viscosity, Reynolds number, and expected Kolmogorov scale.

4.1 Model methodology

To model pinches from each chosen frame, experimental values of flow speed, areal density, pinch current, and pinch diameter are collected at the corresponding experiment time. Flow speed is measured by the time required for light-emitting structures to cross the field of view, where the field of view is measured using known distances. For views perpendicular to the Z-axis, the length of the tripping probe sting is used. For oblique views of the downstream portion of the assembly region, the distance between the tripping probe mast and the outer electrode endwall was used.

Flow speeds ranged from 50–96 km/s, which corroborate well with spectroscopic measurements performed for similar run conditions. Time-resolved areal density is measured by an interferometer beam parallel to the X-axis that crosses the Z-axis 16 cm upstream of the tripping probe mast at Z = 7 cm (figure 4.1). The density measurement used for an image is tracked backwards in time from the frame exposure time to when the plasma structure would have been at Z = 7 cm, referencing the measured flow speed. Furthermore, density is scaled based on the typical size of plasma structures at Z = 7 cm. Figure 4.2 depicts visible emission of the pinch in this region where the plasma is most highly confined. Assuming continuity, the density applied at Z = 23 cm is scaled down from the density measured at Z = 7 cm by $n_{i_{P23}} = \frac{n_{i_{P7}} A_{P7}}{A_{P23}}$, where A_{P7} is the cross-sectional area of the pinch determined from the diameter measured in figure 4.2. To convert line-integrated areal density to an average volumetric density, a chord length of 10 cm is assumed for each pulse. At approximately half the diameter of the assembly region, 10 cm is a reasonable chord length for a measurement of line-integrated density.

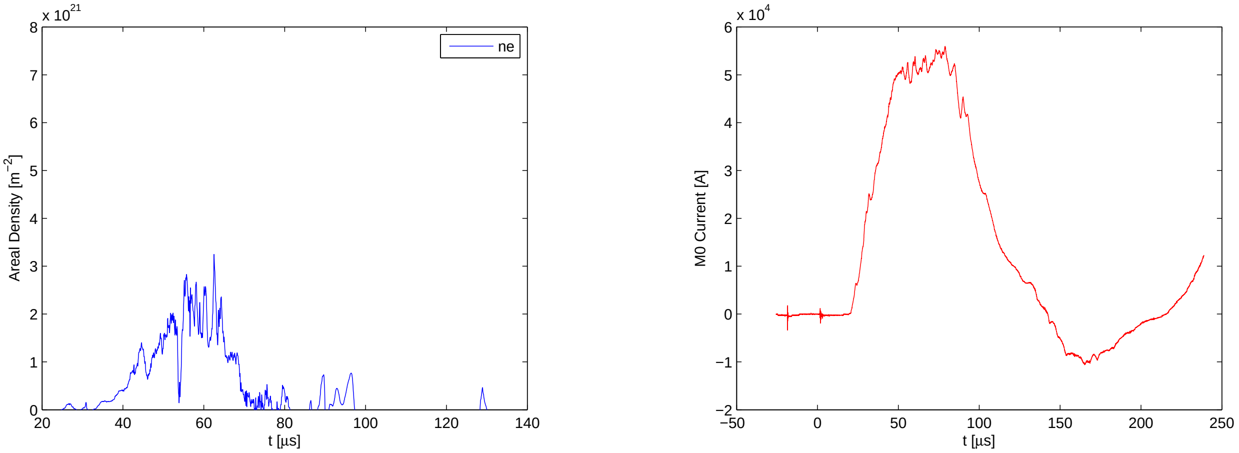

Figure 4.1: On the left is an example of an interferometry signal for measuring n_e, and on the right is pinch current calculated from m = 0 mode data at Z = 20 cm (pulse 141201020).

Pinch current is measured using Fourier decomposed m = 0 mode data at Z = 20 cm, which is a measurement of the magnetic field strength averaged about a set of four azimuthal magnetic

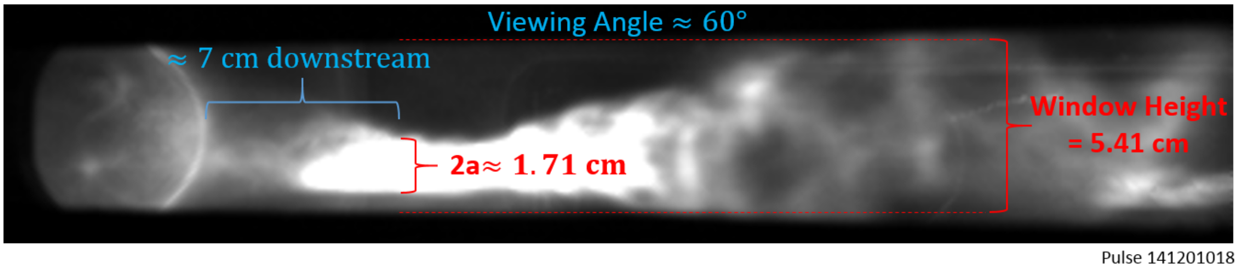

Figure 4.2: Density is measured at Z = 7 cm, where plasma is most highly confined with a pinch radius of 0.85 cm (camera time: 9.70 μs). Note: flow in this image is from left to right.

field probes. The magnetic field strength is converted to a current using Ampere's law, with the radius as that of the inner surface of the outer electrode (figure 4.1). Pinch diameter was measured across regions of visible emission, roughly perpendicular to the Z-axis depending on the pitch of the pinch in the Y-Z plane.

An axisymmetric Bennett equilibrium is assumed for pressure balance $\nabla p = \vec{j} \times \vec{B}$, where

$$B_\theta = \frac{\mu_0 I_0}{2\pi} \frac{r}{r^2 + a^2} \tag{4.1}$$

$$j_z = \frac{I_0}{\pi} \frac{a^2}{(r^2 + a^2)^2} \tag{4.2}$$

$$p = \frac{\mu_0 I_0^2}{8\pi^2} \frac{a^2}{(r^2 + a^2)^2} \tag{4.3}$$

as in [7]. I_0 is pinch current calculated from the $m = 0$ mode data and a is the pinch radius measured in the images.

A density profile is created from equation (4.3), where $n_{i_{profile}} = \frac{p}{2k_b T_i}$ for a uniform temperature T_i. The distribution is scaled to measured experiment conditions by setting the average of the profile to the measured average volumetric density along the interferometry chord length, or $n_i = n_{i_{profile}} \frac{\overline{n_{e_{meas}}}}{\overline{n_{i_{profile}}}}$ assuming a Z=1 plasma where $n_i = n_e$. An example density profile is shown in figure 4.3. From here, iterations on T_i are performed until the Bennett pressure profile (ultimately from pinch radius and current measurements) closely match the $P = 2n_ik_bT_i$ pressure profile (ultimately from density measurements and an assumed ion temperature), as shown in figure 4.3. The largest eddy size l is assumed to be the diameter of the turbulence tripping probe mast where the majority of turbulence is initiated.

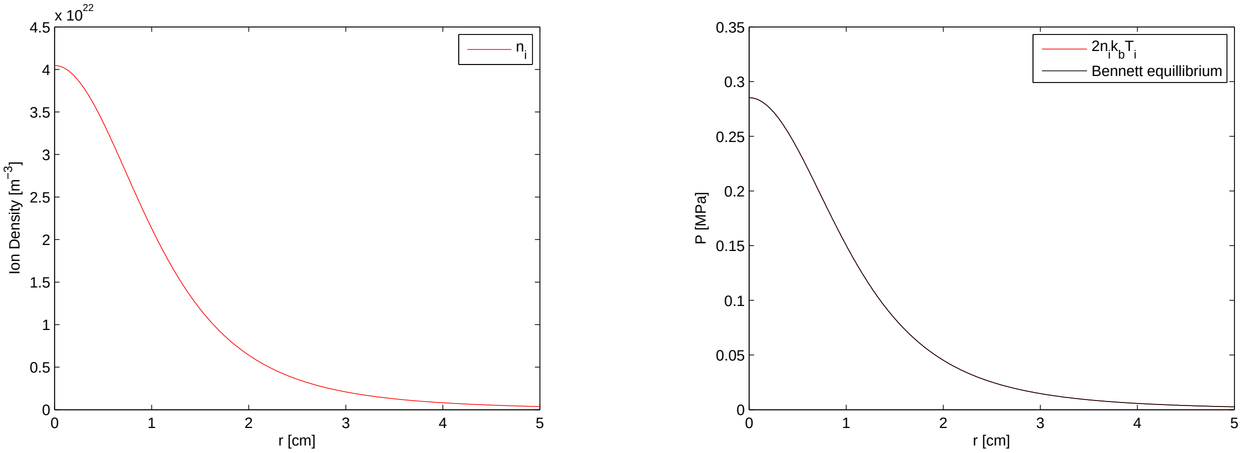

Figure 4.3: On the left is a model of pinch density, and on the right is a plot of equalized magnetic and particle pressures for a measured pinch radius $a = 1.63$ cm and an assumed uniform $T_i = 22$ eV (pulse 141201020).

4.2 Kolmogorov scale

The following examples are three of the most ideal images for the smallest resolvable turbulent structures in the plasma flow, selected from a pool of 12,032 images. The structures are chosen for the turbulent manner in which they are born as eddies broken off of larger plasma structures. The blobs do not further break up, but instead diffuse into undefined homogeneous flow with lower intensity light emission, as though viscous dissipation is responsible for their deterioration. Vorticity was not recorded in these encounters due to its low observability in the images, which are from the perspective shown in figure 4.4 and are in false color to enhance contrast. Unfortunately, the largest anticipated Kolmogorov scales (0.3–0.7 mm) lie below the measured diameters of the smallest light-emitting structures (1.65–2.3 mm). The anticipated scales challenge the resolution of the camera at the given viewing distance, as the projected pixel width is comparable to the expected Kolmogorov scale. To avoid misidentification, a spatial resolution of at most half the expected feature size is required to properly identify the smallest turbulent structures.

The selected images are accompanied by plots that show a peak in density and magnetic field strength at the center and radius of the pinch, respectively. In response, viscosity decreases with radius and Reynolds number increases for all plots except figure 4.16, which shows a different *Re* dependence near the pinch axis. This difference is attributed to a relatively smaller pinch radius measured aft of the tripping probe which required less density scaling from where density is measured at Z = 7 cm. The resultant density profiles shown in figure 4.15 are an order of magnitude higher than in sets 1 and 2. Higher density requires lower ion temperatures to match particle and magnetic pressures, which in turn drives a high unmagnetized Reynolds number $\left(Re \sim \frac{n_i}{T_i^{5/2}}\right)$. The *Re* profile in figure 4.16 approaches the values of sets 1 and 2 in the magnetized region where the magnetic field becomes a dominant factor $\left(Re_\perp \sim \frac{T_i^{1/2} B^2}{n_i}\right)$. The plots are likely most accurate in this region, as the experiment's magnetic field strength values are the most reliable measurements used in this model.

At a glance, Reynolds numbers are lower than the flow qualitatively appears given its turbulent nature. Relative to air, the low mass density of plasmas in ZaP-HD (and most other plasma devices) contribute to small *Re* $\left(Re = \frac{\rho\, l\, u}{\mu}\right)$, despite high flow velocities. The qualitative comparison of ZaP-HD plasmas to flows with similar Reynolds numbers but at terrestrial velocities and atmospheric densities may not be appropriate.

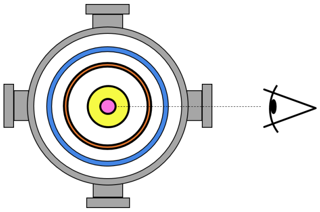

Figure 4.4: Schematic of camera viewing angle, where plasma flow (+z) is out of the paper, or from the viewer's right to left.

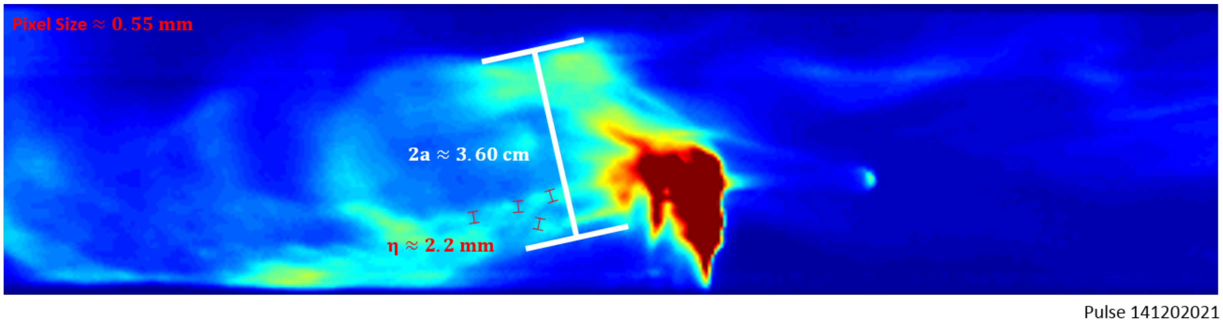

Figure 4.5: Set #1. The smallest light-emitting structures here are approximately 2.2 mm in diameter, with a pinch diameter of 3.6 cm. Each pixel spans approximately 0.55 mm (camera time: 8.75 μs).

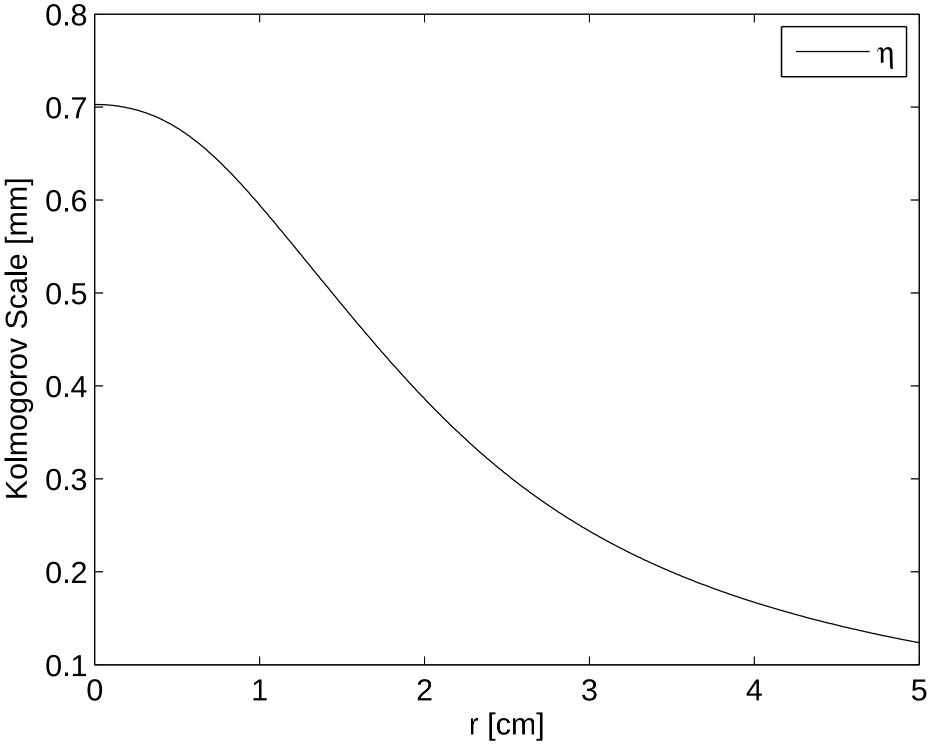

Figure 4.6: Set #1. Expected Kolmogorov scale calculation performed for figure 4.5.

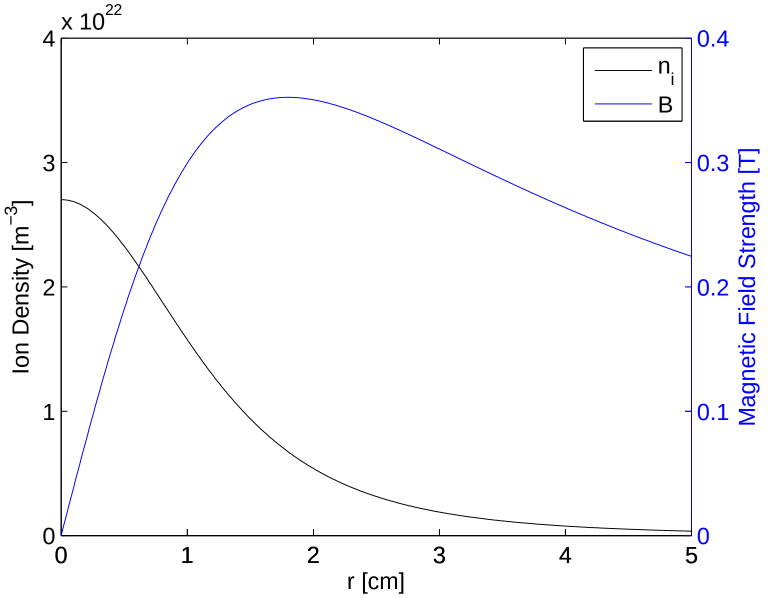

Figure 4.7: Set #1. Density and magnetic field strength calculated for figure 4.5. A uniform $T_i = 23$ eV is used to equate magnetic and particle pressures.

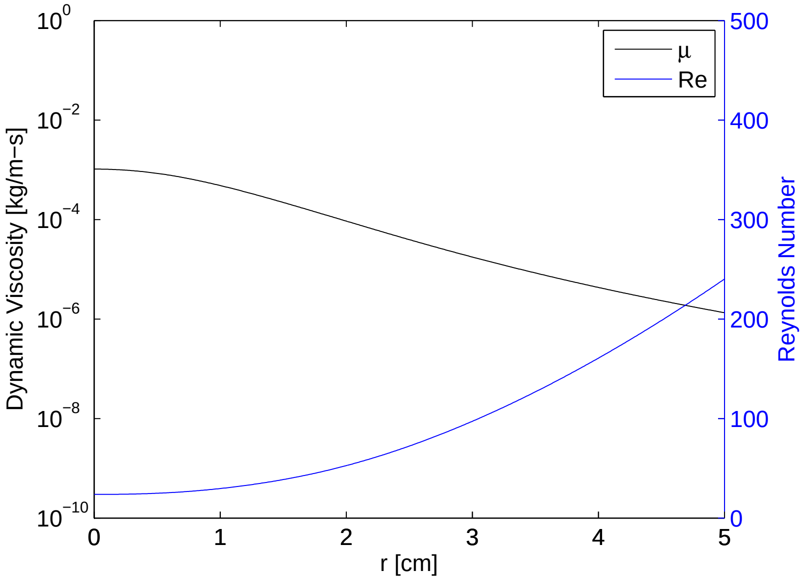

Figure 4.8: Set #1. Fluid viscosity and Reynolds number calculated for figure 4.5.

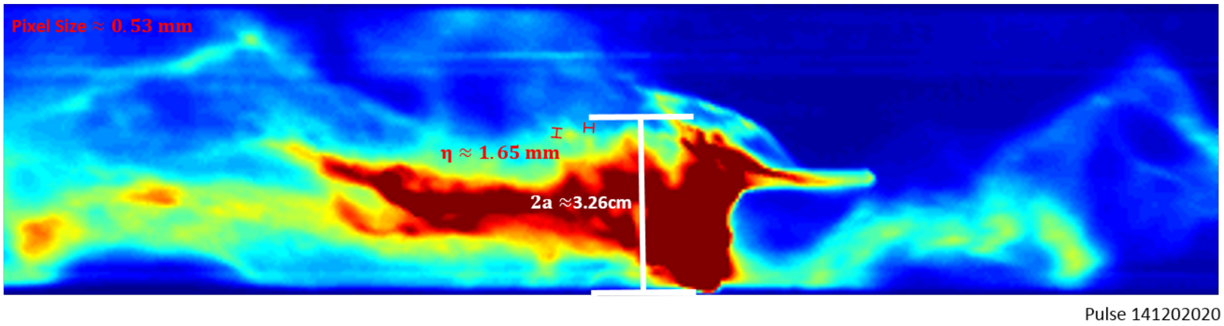

Figure 4.9: Set #2. The smallest light-emitting structures here are approximately 1.65 mm in diameter, with a pinch diameter of 3.26 cm. Each pixel spans approximately 0.53 mm (camera time: 24.17 μs).

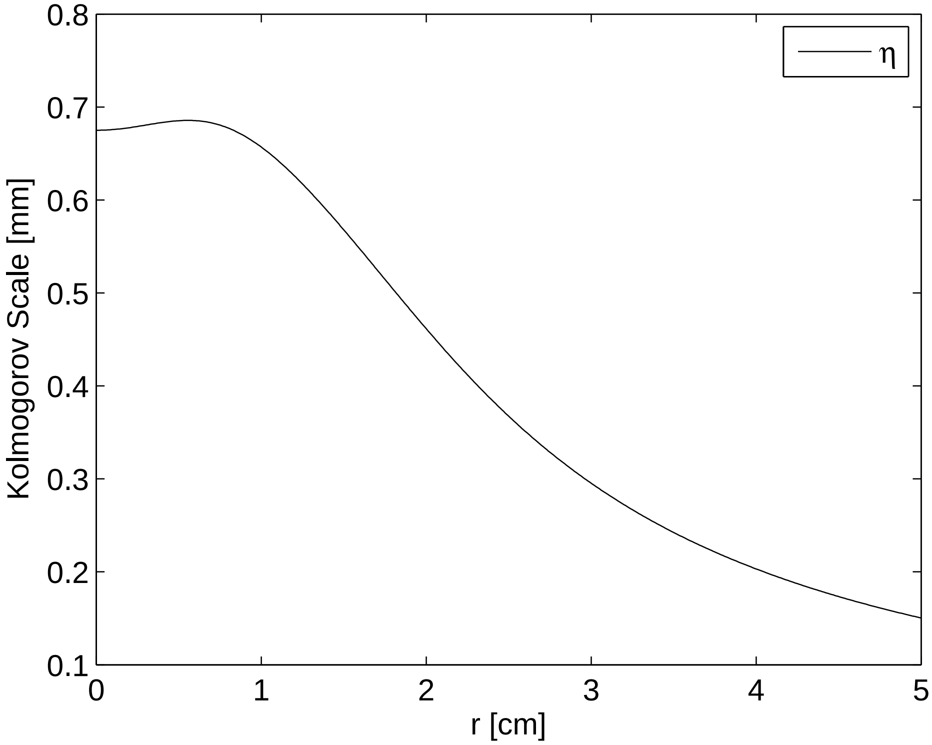

Figure 4.10: Set #2. Expected Kolmogorov scale calculation performed for figure 4.9.

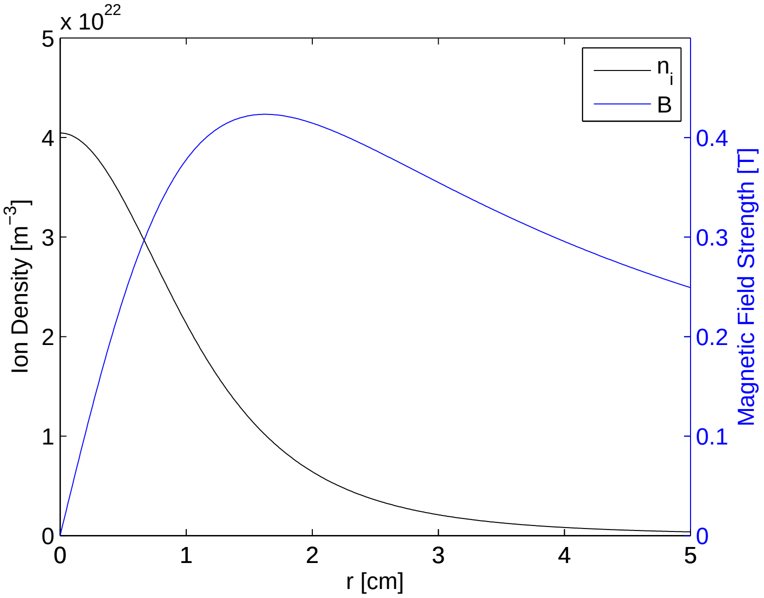

Figure 4.11: Set #2. Density and magnetic field strength calculated for figure 4.9. A uniform $T_i = 22$ eV is used to equate magnetic and particle pressures.

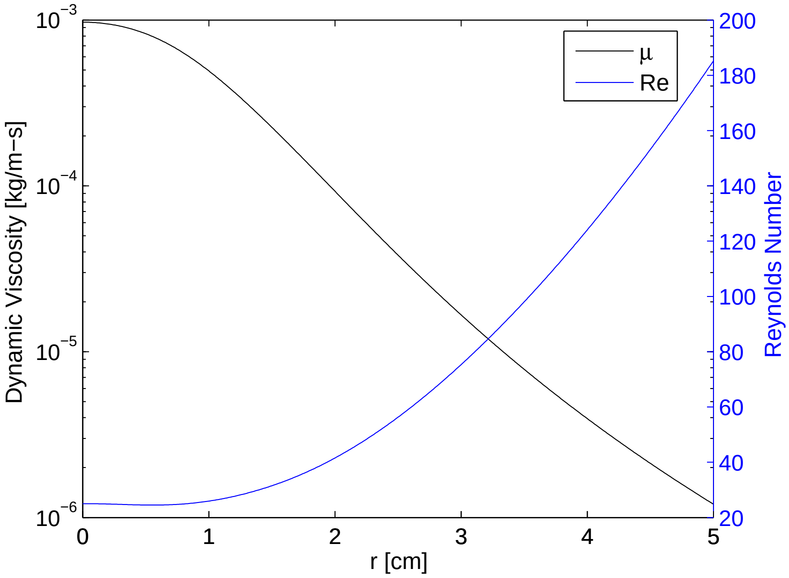

Figure 4.12: Set #2. Fluid viscosity and Reynolds number calculated for figure 4.9.

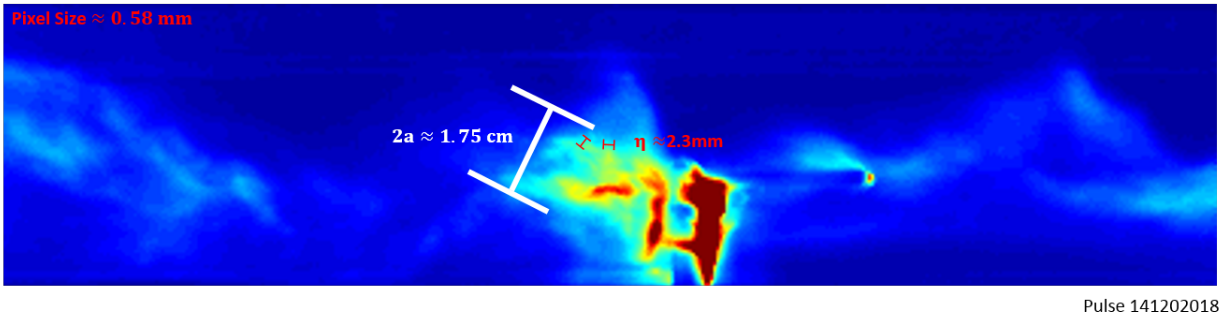

Figure 4.13: Set #3. The smallest light-emitting structures here are approximately 2.3 mm in diameter, with a pinch diameter of 1.75 cm. Each pixel spans approximately 0.58 mm (camera time: 22.49 μs).

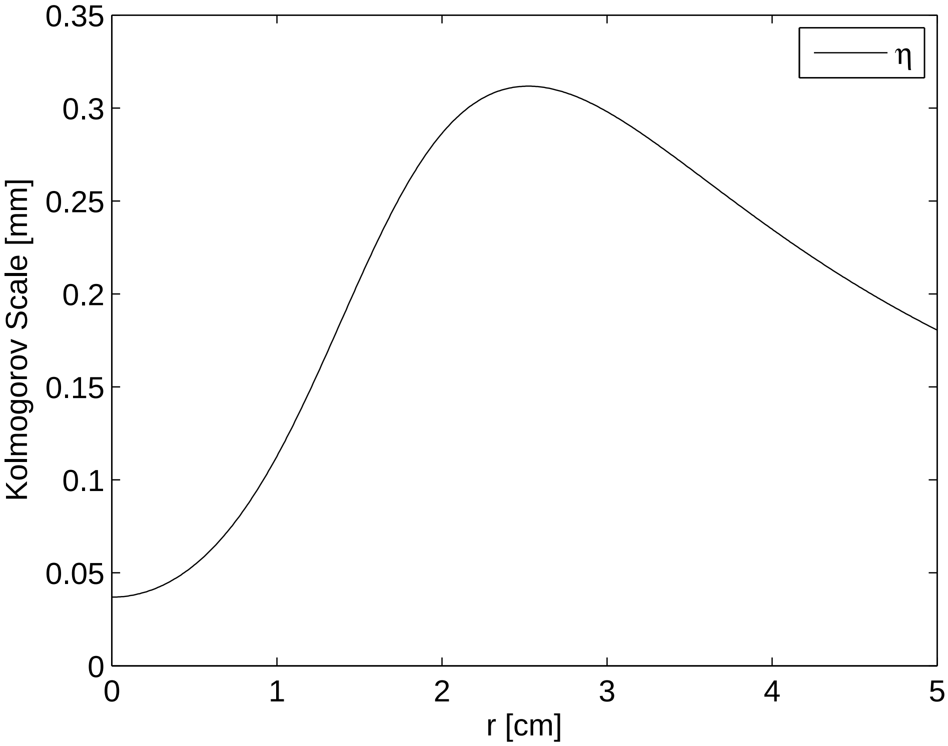

Figure 4.14: Set #3. Expected Kolmogorov scale calculation performed for figure 4.13.

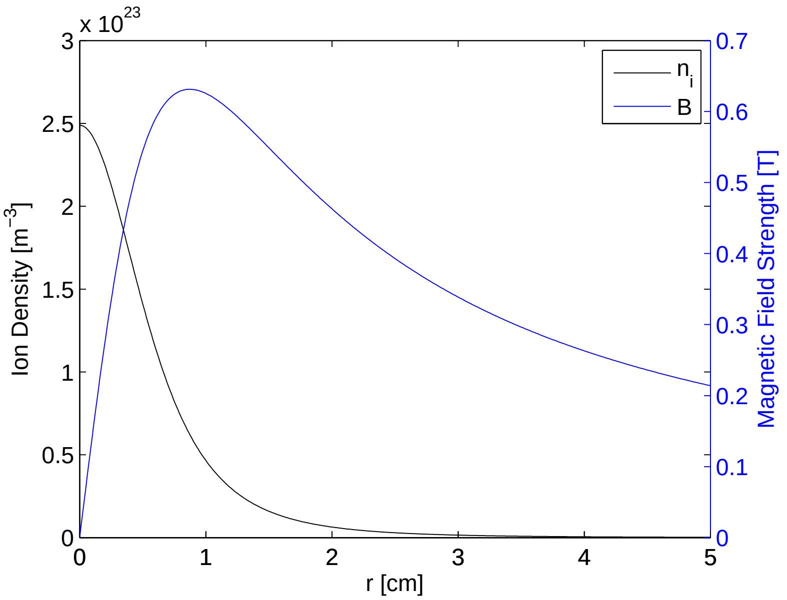

Figure 4.15: Set #3. Density and magnetic field strength calculated for figure 4.13. A uniform $T_i = 8$ eV is used to equate magnetic and particle pressures.

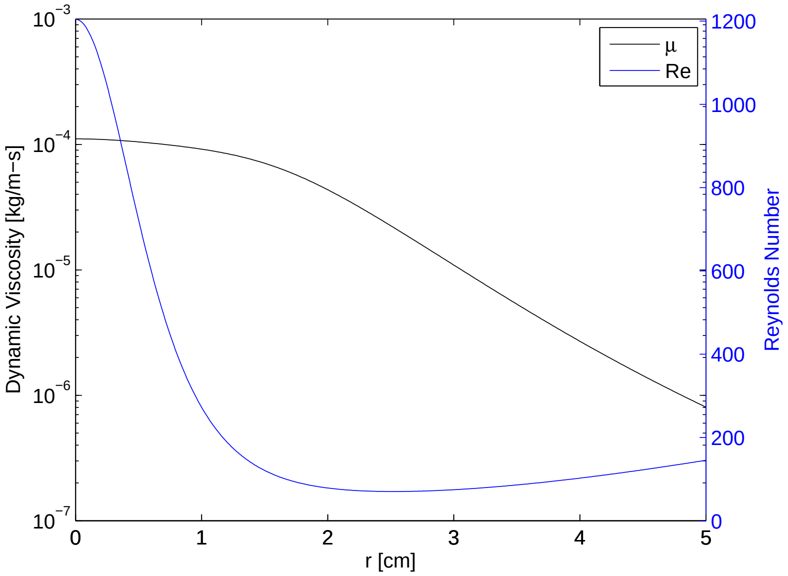

Figure 4.16: Set #3. Fluid viscosity and Reynolds number calculated for figure 4.13.

4.3 Viscous damping time

As shown in section 3.3, interactions with the tripping probe must be laminar to be eligible for viscous damping time analysis. Laminar interactions were only found during pinch formation ($\approx$ 14 μs after the compression bank is triggered), and the best two examples are shown here. Since velocity gradients are difficult to measure with the camera, the diffusion of light-emitting regions of the plasma is observed as a substitute for tracking velocity gradients. Though this is a grand assumption, it is based on the understanding that a laminar diffusion of velocity involves less vorticity and more bulk advection than the diffusion of velocity by turbulent mechanisms.

The accompanying plots of viscous damping time τ are computed using values of the characteristic velocity shear L_v at 10% and 50% of the outer diameter of the turbulence tripping probe mast, as well as with a value that meets the measured viscous damping time (shown in red). The value of L_v cannot be measured, but it is assumed that laminar flow past the tripping probe would produce symmetric velocity gradients with characteristic scale lengths no larger than the radius of the tripping probe mast. Though L_v is an uncertainty in the model, these bounds show that the model and experimental results are in reasonable agreement.

In set #1, a local velocity gradient is induced in the plasma as it passes the tripping probe mast. From there, a dumbbell-shaped distribution of light emission appears that evolves into a diffuse structure over the next two frames.

In set #2, a “hole”, or a structure similar in shape to a vortex ring appears in the pinch after it flows over the tip of the turbulence tripping probe. Over the next four frames it loses definition until it is no longer visible. It is proposed that the diffusion of velocity occurs on a similar timescale as the diffusion of light-emitting particles that form the structure of the “hole”.

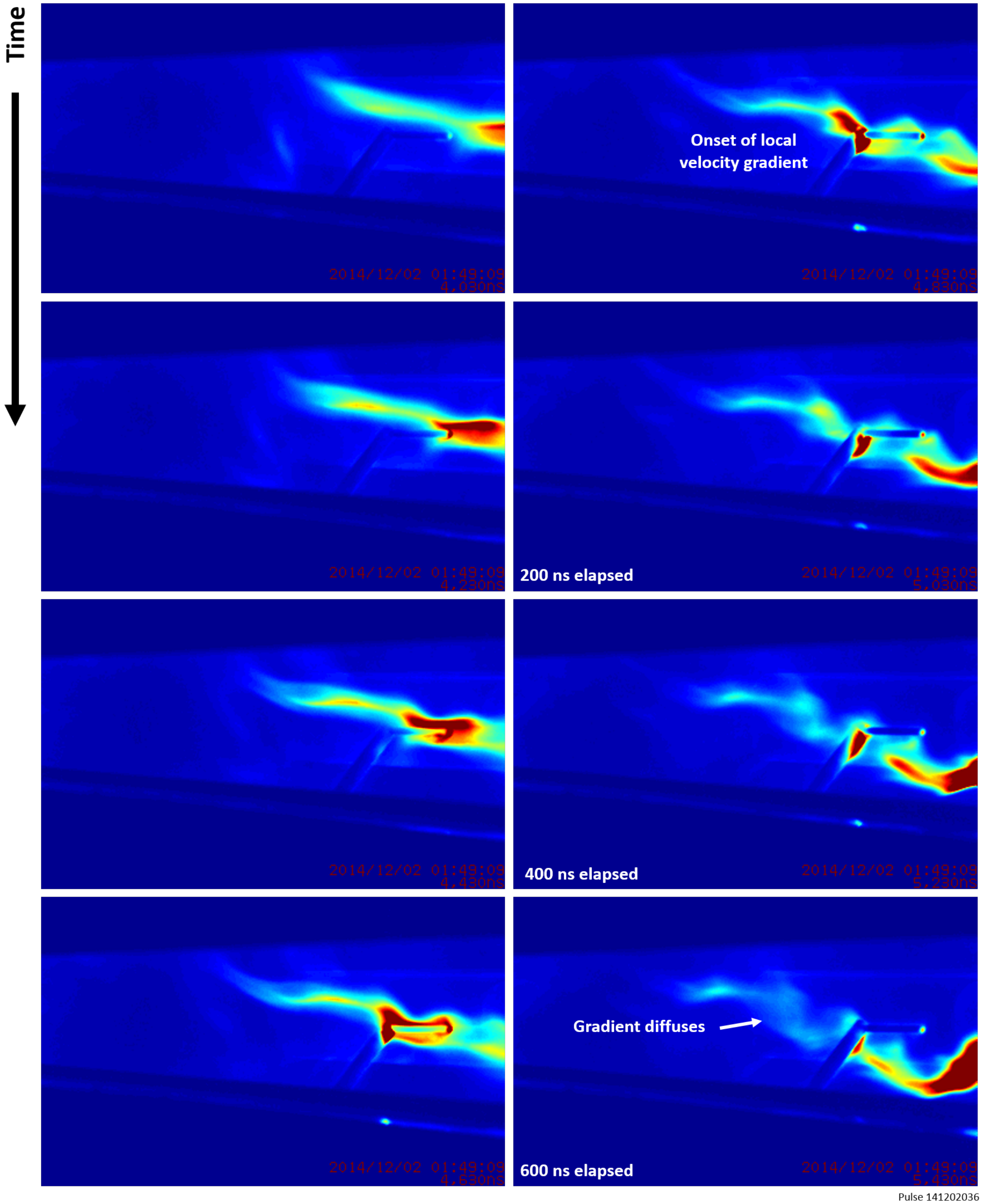

Figure 4.17: Set #4. Viscous dissipation of a velocity gradient induced by the tripping probe mast occurs in approximately 600 ns (5M FPS framing speed).

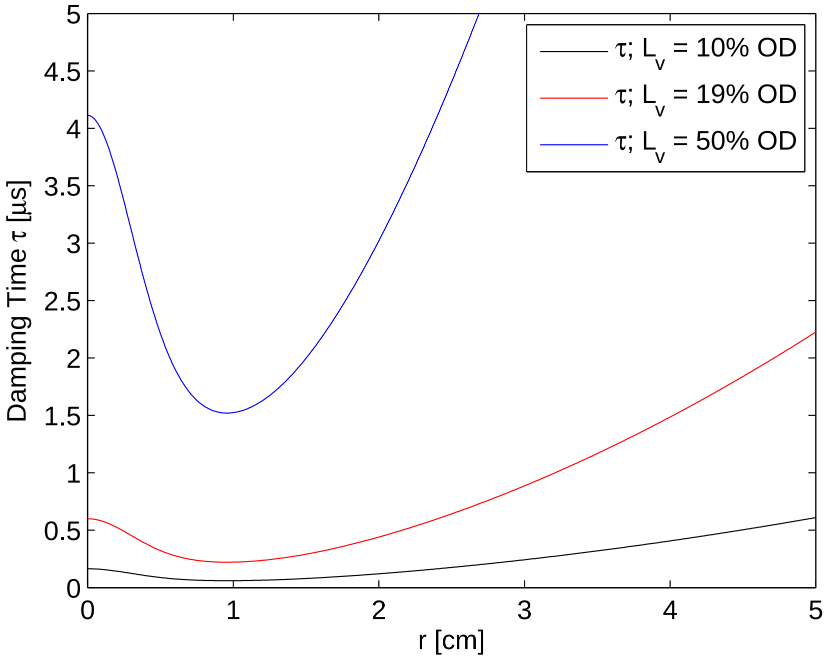

Figure 4.18: Set #4. Viscous damping times calculated for figure 4.17.

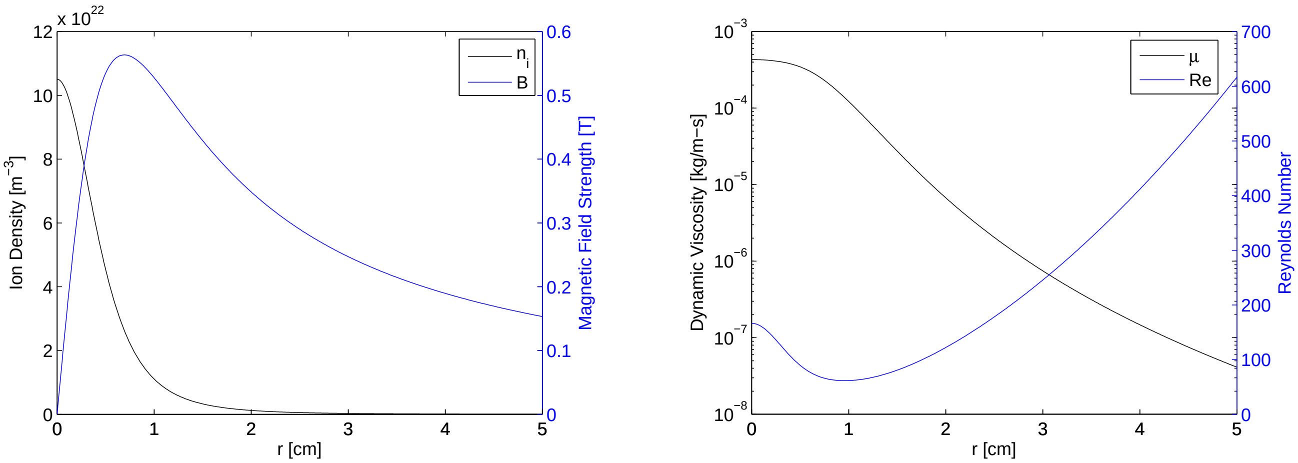

Figure 4.19: Set #4. Density, magnetic field strength, viscosity, and Reynolds number calculated for figure 4.17. A uniform $T_i = 15$ eV is used to equate magnetic and particle pressures.

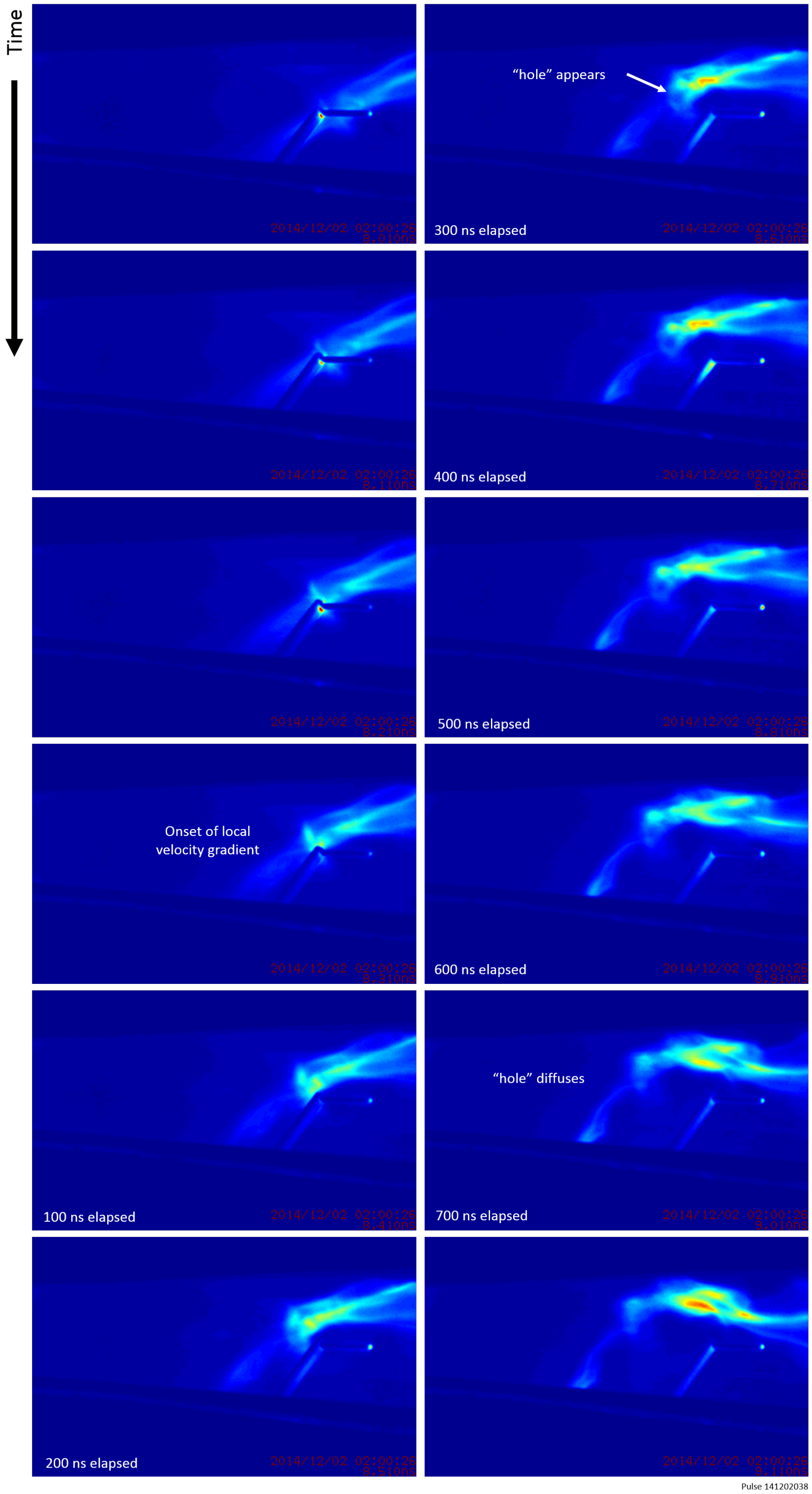

Figure 4.20: Set #5. Viscous dissipation of a velocity gradient induced by the tripping probe mast occurs in approximately 700 ns (10M FPS framing speed).

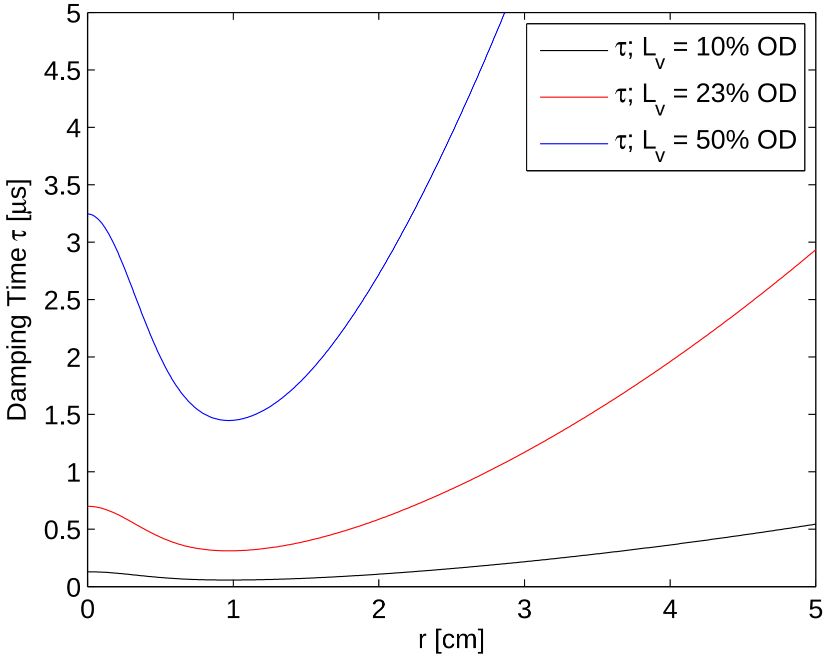

Figure 4.21: Set #5. Viscous damping times calculated for figure 4.20.

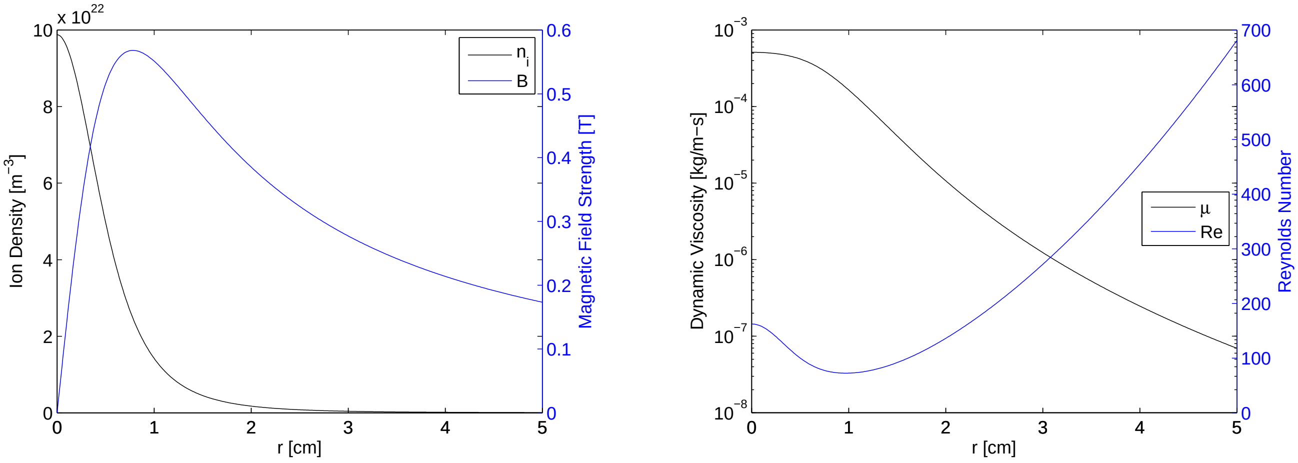

Figure 4.22: Set #5. Density, magnetic field strength, viscosity, and Reynolds number calculated for figure 4.20. A uniform $T_i = 16$ eV is used to equate magnetic and particle pressures.

Chapter 5

DISCUSSION

As previously mentioned, the data used in this investigation was collected during a period of parameter space characterization for the new ZaP-HD machine. Downstream of approximately Z = 15 cm, the pinch rapidly kinked with current connections opening and closing as pinch structure deteriorated and re-formed in the assembly region. A well-centered pinch had not yet extended down the length of the assembly region, and kinks may have contributed to mixing of the sheared flow profile across the pinch radius. Clearly, these conditions were non-ideal for characterizing the effectiveness of the turbulence tripping diagnostic by way of agreement with a simple pinch model, and any agreement found must be considered in the context of the assumptions used in the investigation.

5.1 Kolmogorov theory applicability

Kolmogorov's theory of 1941 has several prerequisites for its proper application to turbulent flows. Noteworthy requirements include high Reynolds number flow, constant density flow, statistically similar small eddies, and vorticity in turbulent structures. The first condition is unlikely to be met in ZaP-HD, as Reynolds numbers are expected to remain below 10^4 as the experiment scales to higher currents and temperatures. The second condition is not isotropically met in any Z-pinch, but in well-structured pinch, density may be assumed constant along the Z-axis and about the azimuthal profile. The third and fourth conditions may be met in ZaP-HD, but were not resolved with the high speed camera used in this study. Vorticity is particularly difficult to quantify as there are no observable particles to track for velocity information. Velocity may be measured by the motion of light-emitting "blobs", but ionization fronts may be confused with plasma advection, and the blobs most strongly emit light due to neutral emission which surrounds plasma but is not plasma itself. These problems plague the use of fast framing photography as a plasma diagnostic in general.

5.2 Suspected boron nitride ablation

Interactions with the tripping probe were qualitatively diverse in the 50 pulses captured with the HPV-X camera, even at various times within the same pulse. Generally, flow exhibited laminar characteristics early in the pulse that transitioned to turbulent flow later in time. It is suspected that boron nitride ablation is responsible for this transition. As the tripping probe absorbs energy from the plasma, boron nitride may ablate from the tripping probe, increasing ion density and lowering ion temperature. Reynolds number scales as $Re \sim \frac{n_i l u}{T_i^{5/2}}$ in unmagnetized plasma and $Re_\perp \sim \frac{T_i^{1/2} B^2 l u}{n_i}$ in magnetized plasma. For a well-centered pinch, boron nitride ablation from tip of the tripping probe mast and sting would be deposited to the unmagnetized center of the pinch where it would increase the Reynolds number, perhaps beyond $Re = 10,000$, the commonly defined mixing transition point where turbulent flow begins in earnest [3]. The difference in typical flow behavior between the beginning and middle of a pulse is shown in figure 5.1.

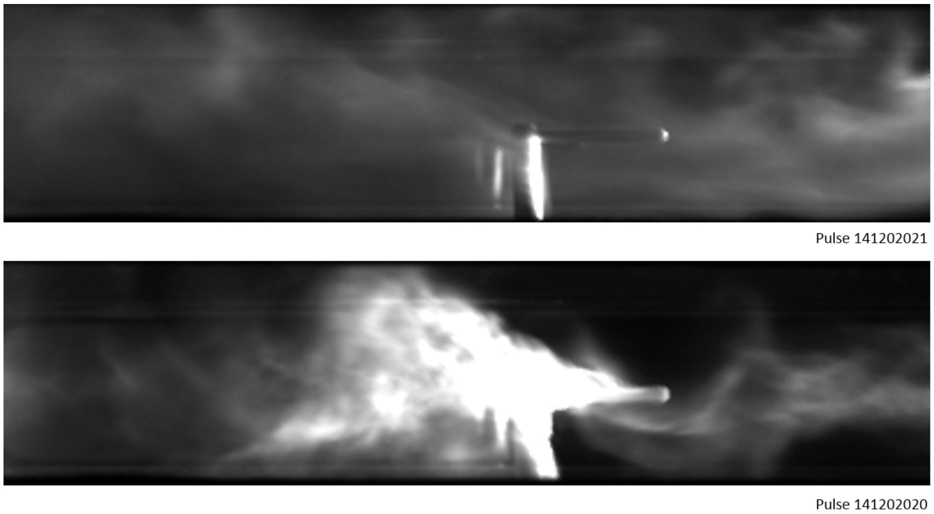

Figure 5.1: Comparison of laminar (top) and turbulent (bottom) flow past the tripping probe. Boron nitride ablation may be responsible for this behavior.

5.3 Recommendations for future work

The ZaP-HD experiment's run parameters have improved since data were collected for this study, and the recent installation of electrically isolated measurement equipment for the middle electrode's magnetic field probes will aid in understanding the behavior of plasma currents in the machine's acceleration region for further optimization. Once the experiment produces highly confined quiescent flow Z-pinches, the measurement of plasma viscosity with fast framing photography may be reconsidered. The author wishes to convey the following recommendations for such a study.

The greatest obstacle in capturing the Kolmogorov scale is camera resolution. For any high speed camera, the projected dimensions of each pixel may be improved with a zoom lens and higher proximity to the plasma in order to target regions where the Kolmogorov scale may be resolved with ease. Although the spatial resolution of the Shimadzu HPV-X is relatively low, the time resolution is extremely helpful for tracking the evolution of turbulent structures.

To distinguish between neutral emission and plasma continuum radiation, a bremsstrahlung filter may be affixed to the camera. An ideal bremsstrahlung filter transmits only a small frequency band to isolate all suspected neutral emission lines, but the light intensity of a narrow band of continuum radiation may be too low to photograph in this stage of ZaP-HD. Instead, a relatively large band of light may be observed that excludes the strongest neutral emission lines. When used together, Wratten #58 and #12 filters attenuate light with wavelengths outside of approximately 500–600 nm to guard against H-α (656.3 nm), H-β (486.1 nm), and the most intense boron line emissions.

The pinch model may be refined with better experimental measurements. In particular, passing interferometry beams just upstream and downstream of the pinch would help validate the model's density profile and discern the occurrence of boron nitride ablation. Perpendicular and oblique spectroscopic measurements just downstream of the tripping probe would provide accurate temperature and velocity profiles in the region of interest to drastically improve the model's estimated uniform profiles. Finally, holographic interferometry just downstream of the tripping probe may resolve fine density structures (30 μm resolution) and would not rely on light emission from the plasma. If fired at a fortunate time, the spatially-resolved density measurement captured over a single 2 ns pulse may sharply resolve turbulent structures in the plasma despite any blur by the line-integrated nature of the measurement. When used in corroboration with fast framing photography, there is hope that a Kolmogorov scale will be captured that matches theoretical predictions.

As ZaP-HD scales to HEDLP conditions, the anticipated on-axis Kolmogorov scale remains large enough to be resolved by fast framing cameras with an appropriate lens, but may be difficult to excite with a turbulence tripping probe. Assuming the pinch scales adiabatically, flow Z-pinch characteristics measured on the previous ZaP experiment scale to the conditions shown in table 1.1 with a 150 kA pinch current, using the scaling relations in [11]. As shown in figure 5.2, the Kolmogorov scale length is at least 1/10 mm within 1/10 mm of the pinch axis, but then diminishes below the resolution of even the holographic interferometry system to 3 μm at the pinch radius[1]. A fine diameter turbulence tripping probe sting could be used to induce velocity gradients in the core of the pinch, but extremely high viscosity would rapidly dampen turbulent structures. Furthermore, at these temperatures boron nitride ablation may significantly perturb the plasma, and the mere survival of a small-diameter tripping probe is questionable. The predicted viscous damping times are on the order of hundreds of nanoseconds and would be still be measurable. At the pinch radius, a viscous damping time of 2.7 μs predicts a sheared velocity endurance length of 0.54 m (longer than the length of the assembly region), assuming a 200 km/s flow speed.

---

[1] This analysis assumes a uniform plasma temperature. The inclusion of a temperature profile in the model would increase perpendicular viscosity at the pinch radius, resulting in a larger Kolmogorov scale length.

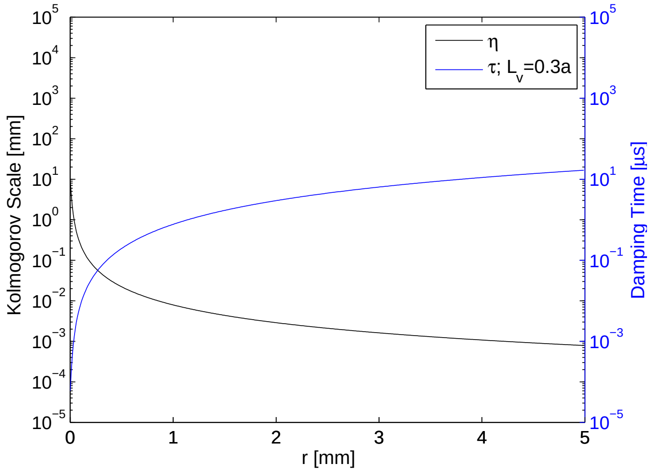

Figure 5.2: Predicted Kolmogorov scale length and viscous damping time for ZaP-HD. Flow speed is assumed to be 200 km/s, the largest eddies in the flow (l) are assumed to be 0.2 mm in diameter, and the characteristic velocity gradient is assumed to be 30% of the pinch radius.

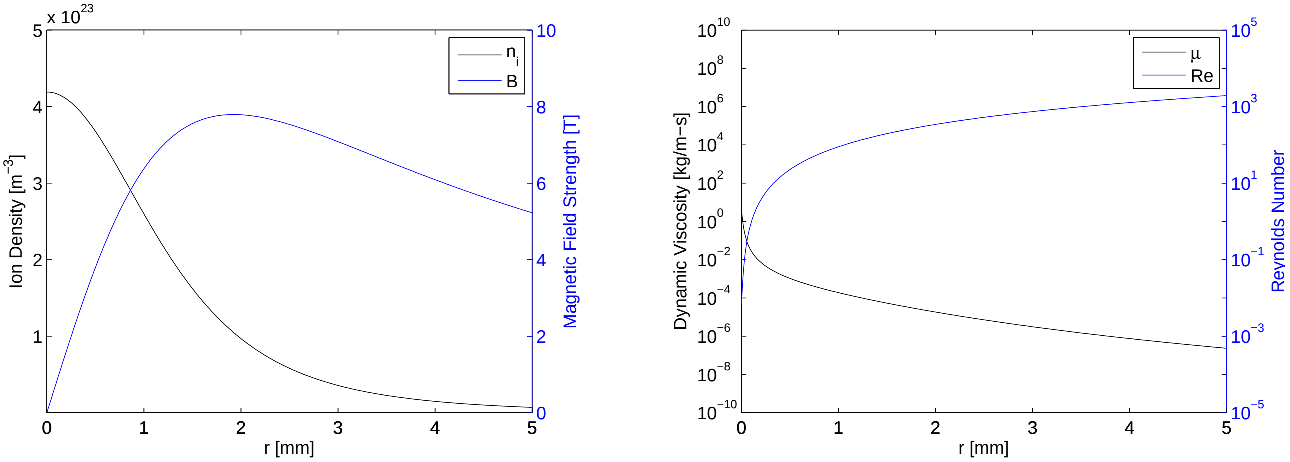

Figure 5.3: Optimal density, magnetic field strength, viscosity, and Reynolds number predicted for the ZaP-HD experiment. A uniform $T_i = 720$ eV is used to equate magnetic and particle pressures.

Chapter 6

SUMMARY AND CONCLUSIONS

In this study, the viscosity of plasma in the ZaP-HD experiment was investigated with fast framing photography by searching for the Kolmogorov scale and viscous damping times of the plasma. The ZaP-HD experiment investigates the stabilizing effect of sheared flow on the classic Z-pinch linear plasma confinement configuration. Plasma viscosity is an important characteristic in the experiment, as it determines the endurance of stabilizing sheared flow profiles in a flow Z-pinch. A measurement of plasma viscosity may be accessed by imaging the smallest turbulent structures, or the Kolmogorov scale, in the flow. A turbulence tripping probe was designed to excite small length scale turbulence in the plasma to determine the feasibility of the diagnostic.

Along the way, a Hadland Imacon 790 fast framing camera was converted from Polaroid film to digital image capture using front surface mirrors, a light-tight box, and a commercial DSLR camera. An accompanying MATLAB code was developed to automatically crop and label the eight images captured in each experimental pulse. The modifications have saved the experiment $2,000 to date in Polaroid film procurement, and will continue to save the lab approximately $3,600 for each year of use. Unfortunately, the camera does not have high spatial or temporal resolution, and is not well-suited to study plasma turbulence. A Shimadzu HPV-X camera was fortuitously demonstrated on the experiment and produced higher resolution imagery, both spatially and temporally, that resolved spectacular turbulent structures in the plasma. However, based on predictions from a simplified pinch model, the spatial resolution was still not high enough to resolve the Kolmogorov scale. As ZaP-HD scales to HEDLP conditions, the Kolmogorov scale will continue to decrease in size and will be difficult to access with a turbulence tripping probe, but there will remain a fine radial region where the Kolmogorov scale may be resolved by fast framing cameras with appropriate lenses if turbulent structures are excited by a small diameter tripping probe.

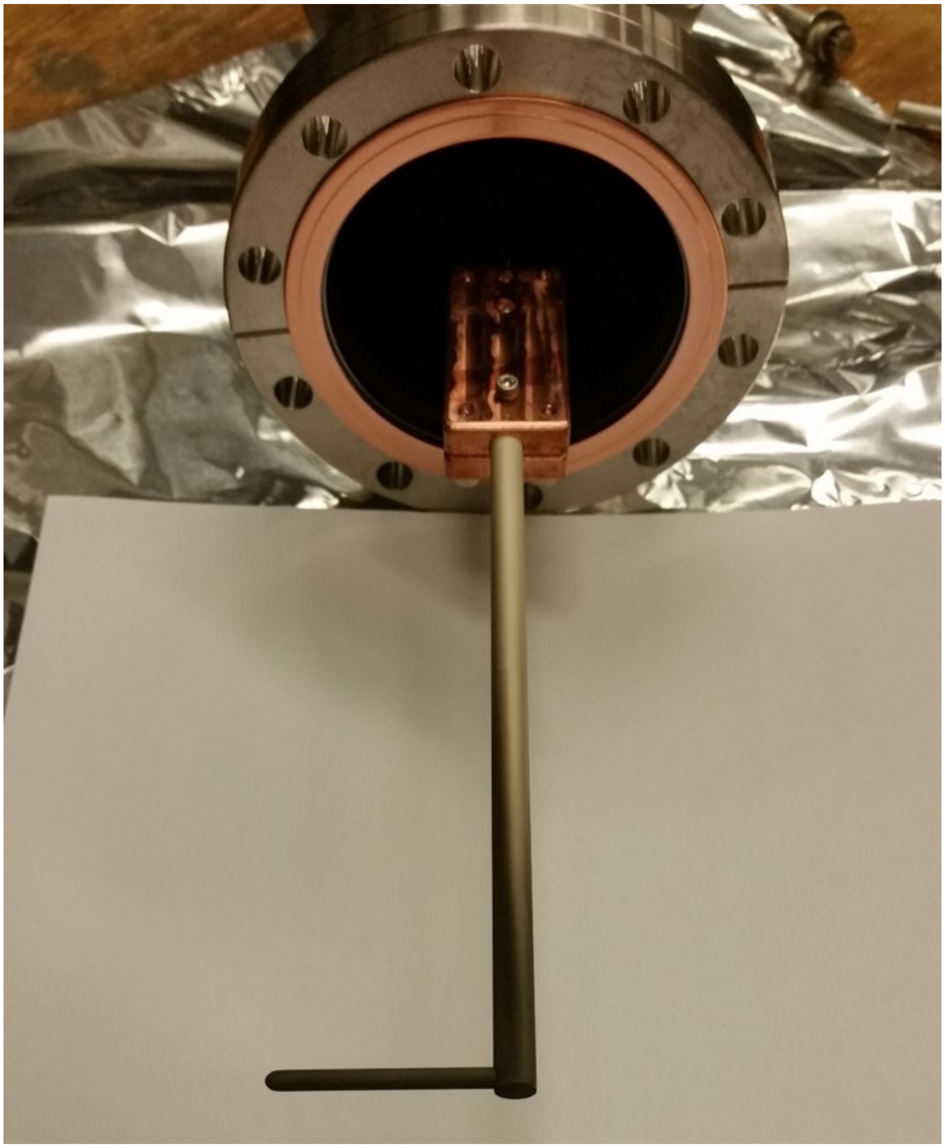

Figure 6.1: The turbulence tripping probe was removed after surviving 50 plasma pulses.

BIBLIOGRAPHY

[1] S.I. Braginskii. Transport processes in a plasma. *Reviews of Plasma Physics*, 1, 1965.

[2] P.A. Davidson. *Turbulence: An Introduction for Scientists and Engineers*. Oxford UP, 2004.

[3] P. E. Dimotakis. The mixing transition in turbulent flows. *J. Fluid Mech.*, 409:69–98, 2000.

[4] A. A. Fridman. *Plasma Physics and Engineering*. Taylor & Francis, 2004.

[5] R.J. Goldston and P.H. Rutherford. *Introduction to Plasma Physics*. Taylor & Francis, 1995.

[6] B.B. Kadomtsev. Hydromagnetic stability of a plasma. *Reviews of Plasma Physics*, 2, 1966.

[7] S.D. Knecht. *Comparison of Electrode Configurations on ZaP: Investigation of Heating Mechanisms in a Flow Z-Pinch*. PhD thesis, University of Washington, 2012.

[8] S.D. Knecht et al. Effects of a conducting wall on z-pinch stability. *IEEE Transactions on Plasma Sciences*, 42(6):1531–1543, 2014.

[9] S.B. Pope. *Turbulent Flows*. Cambridge UP, 2000.

[10] U. Shumlak et al. Advanced space propulsion based on the flow-stabilized z-pinch fusion concept. *AIAA*, (4805), 2006.

[11] U. Shumlak et al. The sheared-flow stabilized z-pinch. *Transactions of Fusion Science and Technology*, 61, 2012.

[12] U. Shumlak and C.W. Hartman. Sheared flow stabilization of the $m = 1$ kink mode in z pinches. *Physical Review Letter*, 75(18):3285, 1995.

[13] L. Spitzer. *Physics of Fully Ionized Gases*. Interscience Publishers, 1962.

Appendix A

USING THE IMACON CODE

A.1 Automated cropping routine

1. Organize images in a folder within “...Dropbox\Photos\Imacon Photos” with the correct date (YYYY-MM-DD).

2. Run MATLAB as administrator.

3. Open the Imacon code folder in MATLAB (“...Dropbox\Photos\Imacon Photos\Code”)

4. In command window, type “init” and press enter.

5. Enter the shot and image file number of the first image to be processed and click “ok”[1].

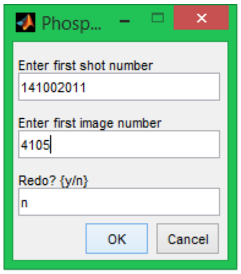

Enter first shot number: 141002011

Enter first image number: 4105

Redo? (y/n): n

6. In the command window, type “run process”. The program will attempt to automatically crop each set of eight images and its frames for individual output as well as create a .gif reel of each shot.

---

[1] If images are being reprocessed, type “y” in “Redo?” and follow the code’s instruction to disable line 78 in “process.m”

7. If automated framing fails, program will request input from the user's expert eye (see below).

8. The program will flag "Error using imread...File '...' does not exist" when it runs out of images to process or if there is an image designation mismatch.

A.2 Manual framing process

If the program detects poor framing quality from automated cropping, it will request user assistance. Follow the on-screen instructions to manually frame each image by drawing rectangles with the mouse. Once each rectangle is satisfactorily positioned, double click inside the rectangle. Select the entire set of 8 images first, followed by each frame in the top and bottom rows of the set, from left to right.

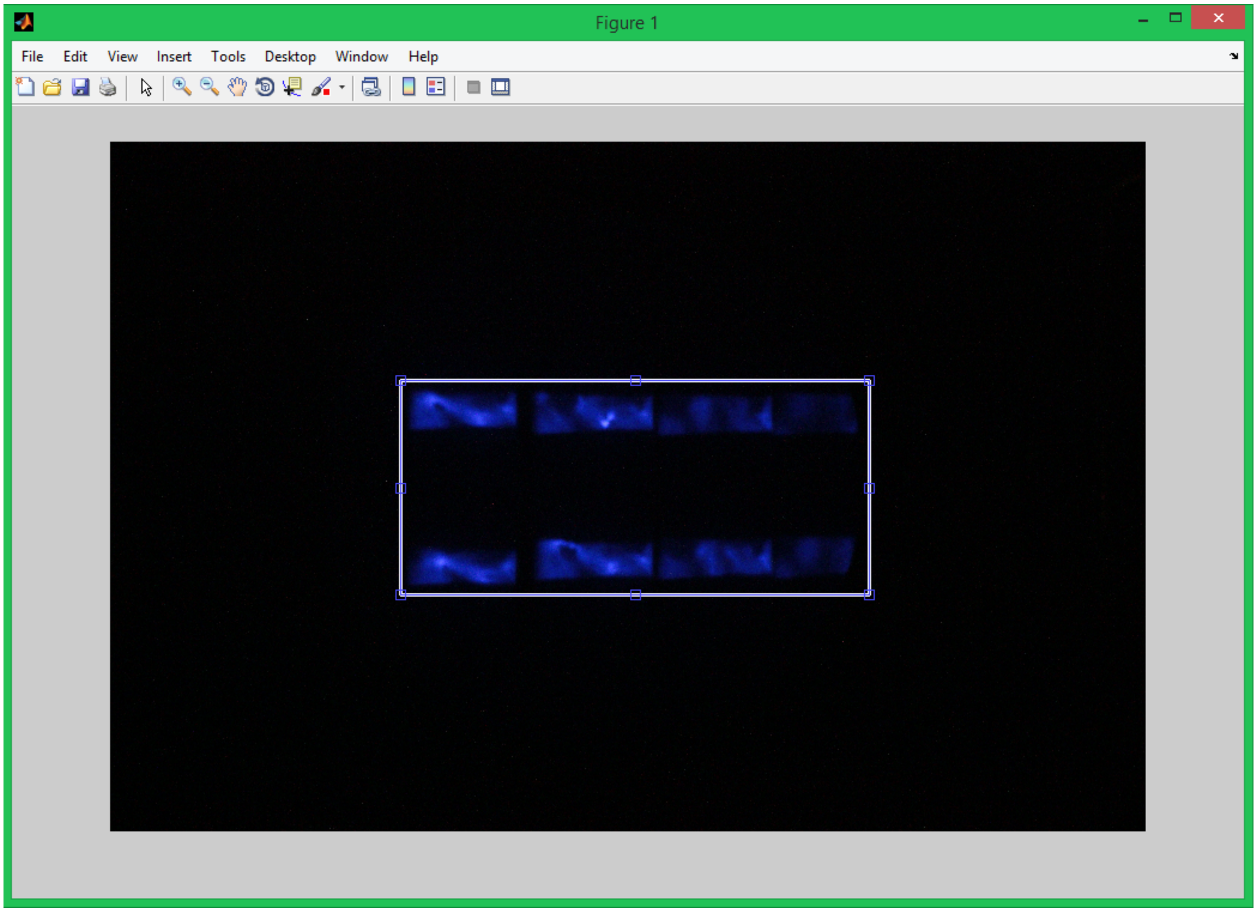

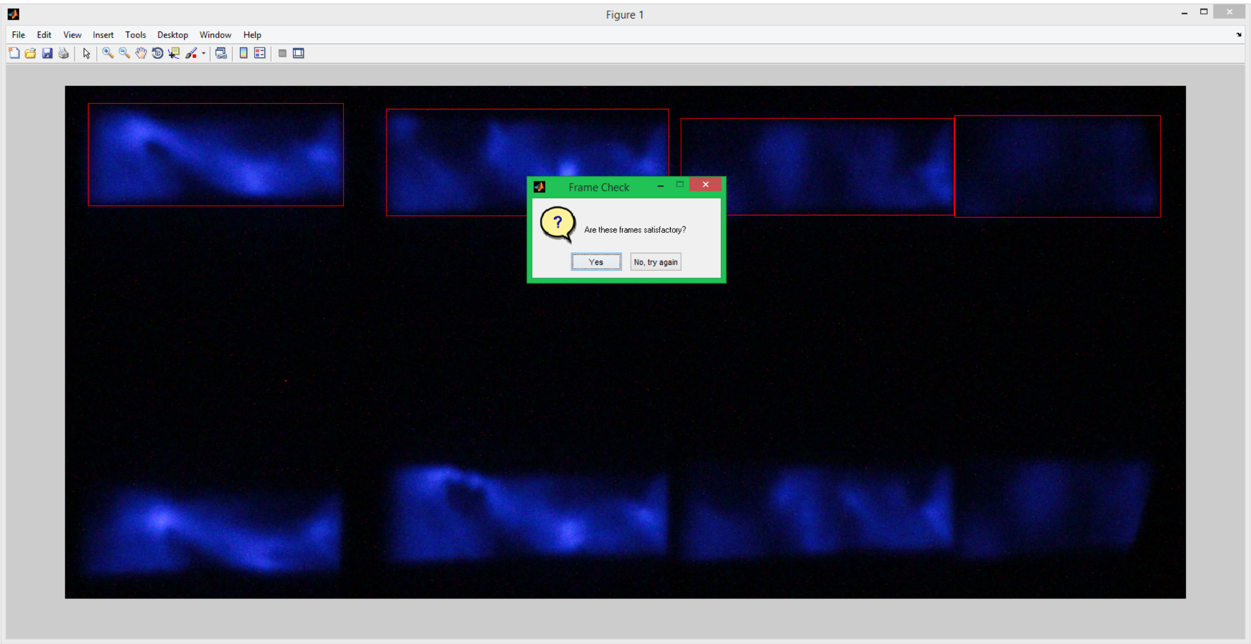

Are these frames satisfactory?

A.3 Configuring code for use on a different computer

The code resides in the ZaP lab's shared Dropbox folder, but it is currently configured to run on a single machine, the Hard Drives Northwest, Inc. computer serial number 166205. It may be modified for other computers by changing a few of the Dropbox addresses in the following lines of code:

- process.m line 11: change "vardir" to the computer's address for the Imacon code folder within Dropbox (the prelude to "...Dropbox\Photos\Imacon Photos\Code")
- process.m line 27: change "directory" to the computer's address for the Imacon photos folder (the prelude to "...Dropbox\Photos\Imacon Photos"). Only alter the address up to "...\20" to avoid an error.

- init.m line 2: change address for variables to the computer's address for the Imacon code folder within Dropbox (the prelude to "...Dropbox\Photos\Imacon Photos\Code\variables.mat")

- init.m line 16: change address for variables to the computer's address for the Imacon code folder within Dropbox (the prelude to "...Dropbox\Photos\Imacon Photos\Code\variables.mat")

Appendix B

TURBULENCE TRIPPING PROBE MACHINE DRAWINGS

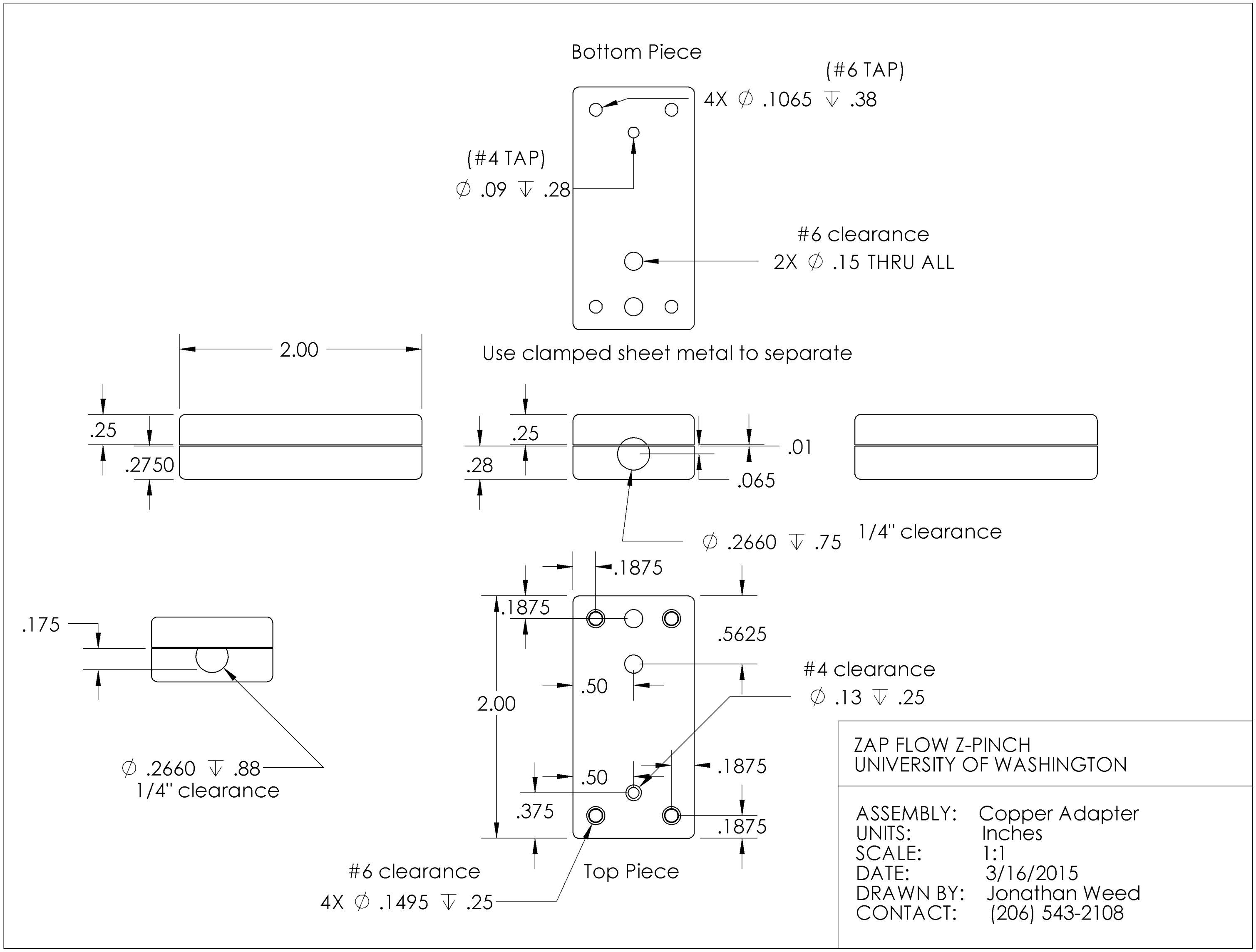

Figure B.1: An adapter to attach the boron nitride mast to a linear translator. Copper was used for its favorable machinability and vacuum properties.

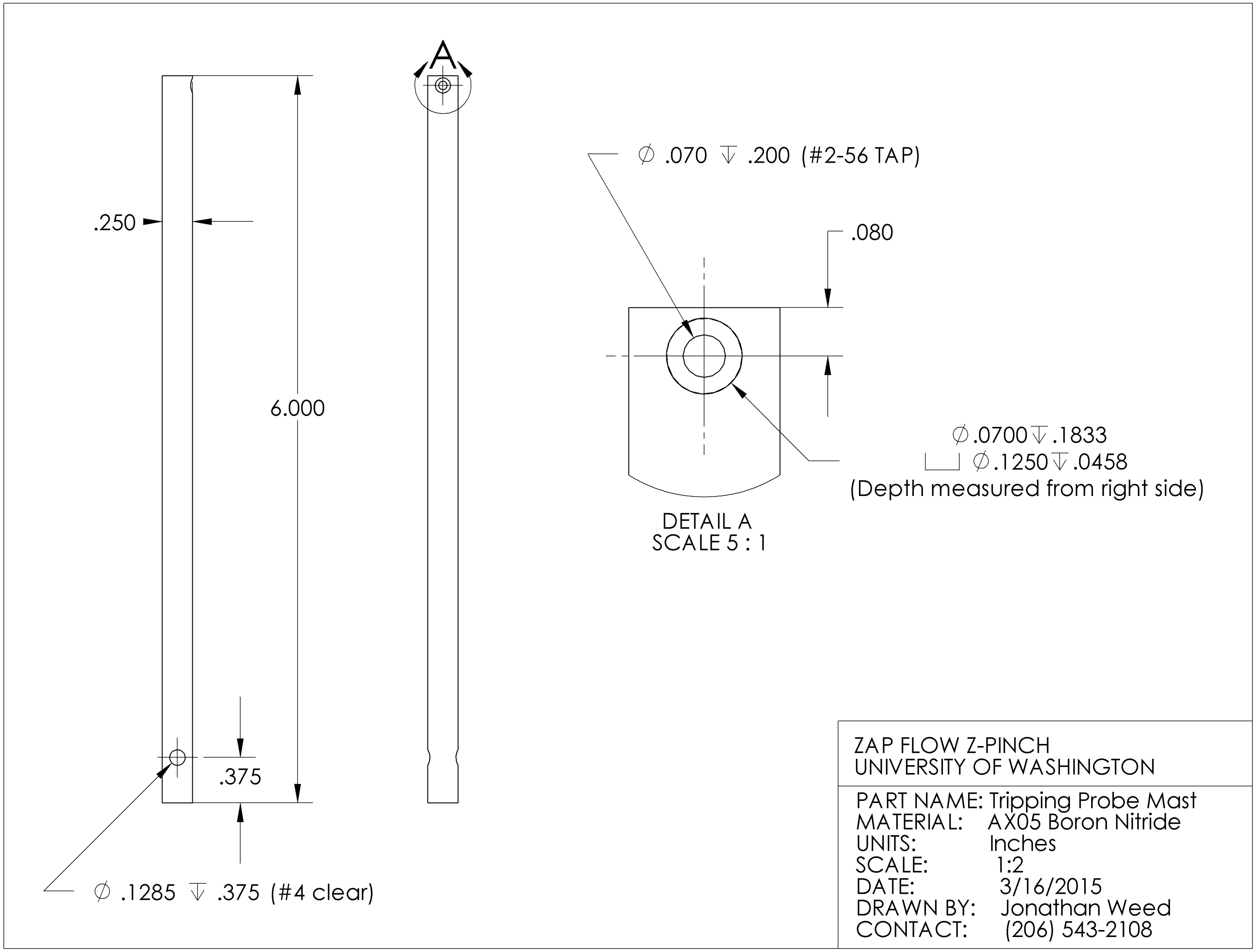

Figure B.2: Boron nitride turbulence tripping probe mast

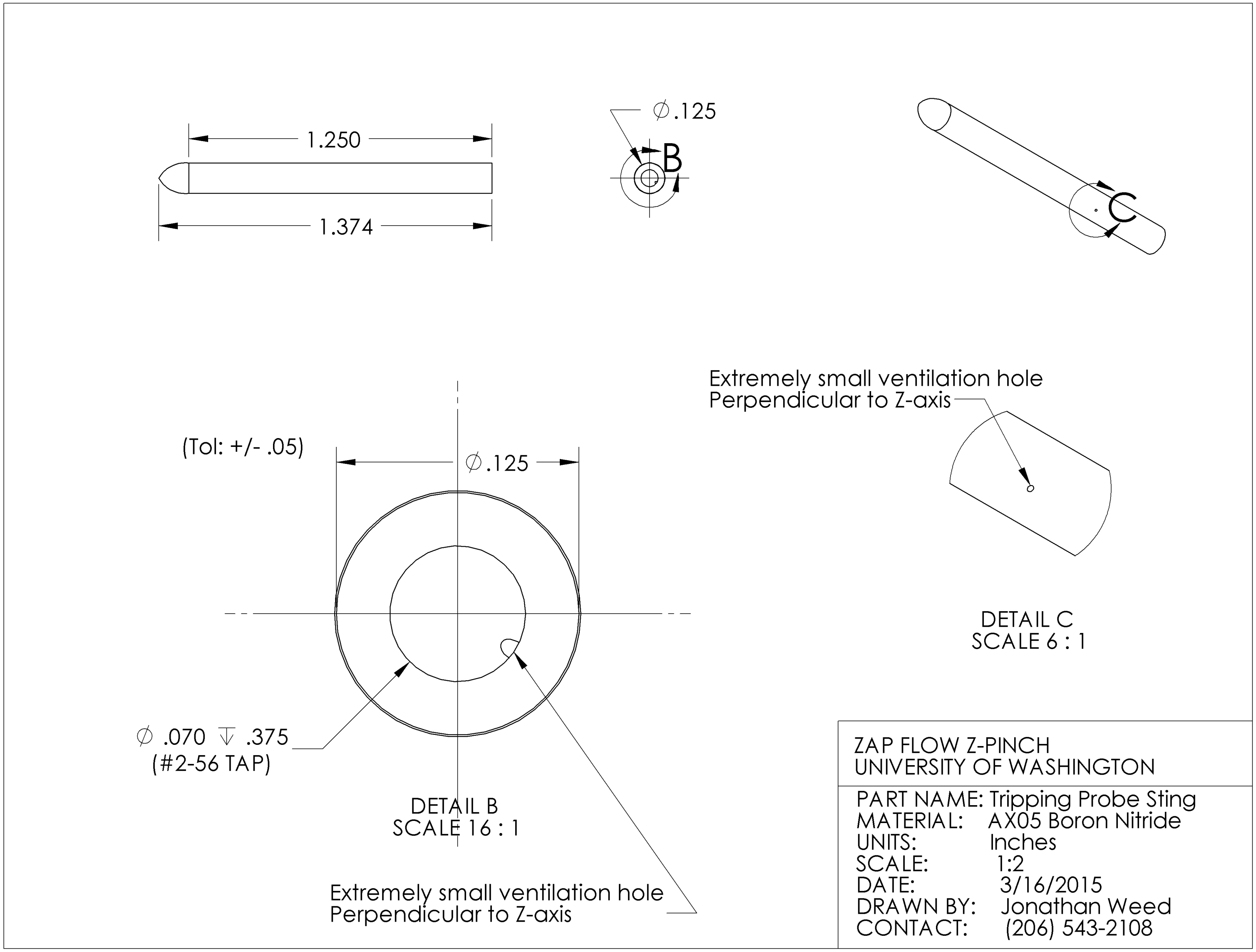

ZAP FLOW Z-PINCH
UNIVERSITY OF WASHINGTON

PART NAME: Tripping Probe Sting
MATERIAL: AX05 Boron Nitride
UNITS: Inches
SCALE: 1:2
DATE: 3/16/2015
DRAWN BY: Jonathan Weed
CONTACT: (206) 543-2108

Figure B.3: Boron nitride turbulence tripping probe sting